Enhanced Methods for Surface Current Estimation from X-Band Radar Data

by

© **Yi Li, B.Eng.**

A thesis submitted to the School of
Graduate Studies in partial
fulfillment of the requirements for
the degree of Master of Engineering.

Department of Electrical and Computer Engineering
Faculty of Engineering and Applied Science

Memorial University

May 2025

St. John's, Newfoundland and Labrador, Canada

Abstract

Estimating ocean surface currents accurately is crucial for a wide range of applications, including marine navigation, environmental monitoring, and coastal management. Traditional methods for measuring surface currents face challenges such as limited spatial coverage and sensitivity to environmental noise, making the development of more accurate and robust techniques a pressing need in oceanography. This thesis focuses on improving the accuracy and robustness of ocean surface current estimation using X-band radar image sequences by introducing two novel algorithms.

In the first part of this thesis, a Symmetry of Doppler Shifts (SDS) method is introduced for retrieving surface current information from radar images. The method focuses on extracting the wave angular frequencies and corresponding wavenumbers from the radar image sequences. Then, Doppler shifts are calculated based on wavevectors that exhibit symmetry with respect to the origin in the wavenumber plane. These Doppler shifts are used to estimate both the speed and direction of surface currents. Simulations with synthetic data show that the SDS method achieves a root mean square error (RMSE) of 0.13 m/s for current speed and 1.4° for direction. The results indicate that the method performs with accuracy comparable to existing techniques under simulated conditions.

The second part of this research builds on the SDS method by integrating it with an enhanced Polar Current Shell (PCS) algorithm. The improvements include the application of Kernel Density Estimation (KDE) for noise filtering, interquartile range filtering to remove outliers, and symmetry-based noise reduction. The modified PCS method also employs a single curve-fitting process, analyzing all wavenumbers in the PCS domain collectively rather than individually. The improved algorithm was validated with both simulated data and real-world radar data from a Decca radar (2008) and a Koden radar (2017). Results show that the modified PCS method reduces the RMSE for speed by 0.06 m/s and direction by 3.8° for the Decca radar, and by 0.02 m/s for speed and 4.6° for direction for the Koden radar, compared to the original PCS method.

Acknowledgements

This thesis would not have been possible without the help, guidance, and support of many people, and I am truly grateful for their contributions. First and foremost, I would like to thank my supervisor, Dr. Weimin Huang, for his ongoing support and advice throughout this research. His patience and encouragement have been crucial in helping me complete this project, and I am deeply thankful for his guidance.

The work was supported by the Natural Sciences and Engineering Research Council of Canada Discovery Grants under Grant NSERC RGPIN-2024-04442 to Dr. Weimin Huang and the Canada First Research Excellent Fund (CFREF) to Memorial University.

I would also like to express my appreciation to Zhiding Yang for his valuable suggestions and input, which have greatly improved the quality of this work. His feedback and expertise have been incredibly helpful throughout this journey. I want to sincerely thank my colleagues in the Remote Sensing group for their friendship and cooperation. Their support and dedication have made this journey both more enjoyable and meaningful.

Lastly, I want to express my deepest gratitude to my family, especially my parents. Your constant support, love, and encouragement have given me the strength to achieve my goals. I could not have completed this without you.

Table of contents

List of tables

List of figures

List of symbols

This list of symbols includes only the most important symbols to the understanding of the present thesis, indicating the page where the symbol was first used. Local variables used in the derivation of expressions or for the demonstration of definitions were not included.

Symbol	**Description**	**Page**
$\overline{\omega}$	the cut-off frequency	19
$\vec{k}$	wave vector	20
ω_0	the angular frequency in the absence of surface current	20
g	the acceleration due to gravity	20
d	the water depth	20
$\vec{U}$	surface current	21
ω_u	the Doppler shift caused by current $\vec{U}$	21
ω_{u_k}	the Doppler shift corresponding to $\vec{k}(k_x, k_y)$	21
$s_{\omega(k,k')}$	the sum of the Doppler shifts for these two symmetric wave vectors	22
E_{ω_u}	the symmetric wave vector Doppler shift mean absolute deviation (MAD) ratio	22
$S(f)$	the spectral density at frequency f	24
α	an empirical constant (0.0081)	24
f_p	the peak frequency	24

Symbol	**Description**	**Page**
D	the directional spreading function	25
ω	the angular frequency	25
θ	the azimuth angle	25
$\bar{\theta}$	the mean wave direction	25
s	a parameter that controls the angular spreading	25
Γ	the Gamma function	25
f	the wave frequency	25
f_p	the peak wave frequency	25
$s_{\max}$	the maximum value of s	25
μ	a parameter that has different values depending on the wave frequency	25
θ_{ku}	the angle between the current direction and the wave vector direction	35
$f(U, \overline{\theta_{ku}})$	the model function for curve fitting	36
E	the error cost function	36
$\hat{f}_i(x)$	the estimated density at a any point x within the domain of input data	37
$\mathbf{Z}^{'}$	the filtered data in all directions	38
$\bar{f}^{\max}(x)$	the mean max density in all directions	38

List of abbreviations

This list of abbreviations includes all the abbreviations to the understanding of the present thesis, indicating the page where the symbol was first used.

Abbreviations	**Description**	**Page**
ADCPs	Acoustic Doppler Current Profilers	1
VMCM	Vector Measuring Current Meter	1
GDP	Global Drifter Program	2
HF	High-frequency	2
SAR	Synthetic Aperture Radar	2
FFT	Fast Fourier Transform	3
PCS	Polar Current Shell	4
LS	Least Squares	5
ILS	Iterative Least Squares	6
WLS	Weighted Least Squares	6
DiSC	Dispersive Surface Classificator	8
NSP	Normalized Scalar Product	9
CSC	Cross-Spectral Correlation	11
KDE	Kernel Density Estimation	14
IQR	Interquartile Range	14

Abbreviations	**Description**	**Page**
CC	correlation coefficient	14
RMSD	Root Mean Square Deviation	14
SDS	Symmetry of Doppler Shifts	19
3D	Three-dimensional	19
PM	Pierson-Moskowitz	24
SR	Search-and-Rescue	31
WaMos II	Wave Monitoring System II	33
DRDC	Defence Research and Development Canada	50
HH	Horizontal Transmit and Horizontal Receive Polarization	58

Chapter 1

Introduction

1.1 Research Background

The accurate estimation of ocean surface currents is essential for a wide range of maritime applications, including coastal monitoring, marine navigation, and environmental management. Surface currents influence everything from ship routing to the dispersion of pollutants and biological processes. Traditionally, oceanographic measurements of surface currents have been conducted using in-situ instruments like Acoustic Doppler Current Profilers (ADCPs) and drifting buoys. These methods provide point-based data and are widely recognized for their accuracy in calm sea states and clear weather conditions. However, they also suffer from several limitations, particularly in terms of spatial coverage and susceptibility to environmental factors such as rough seas and high wind speeds [1, 2]. Similarly, current meters like the Vector Measuring Current Meter (VMCM) provide precise measurements of the horizontal components of water flow but are limited by their point-based data collection. These instruments are useful for capturing small-scale velocity changes in the upper ocean, though they struggle with rapidly changing currents [3]. Moreover, while the VMCM is robust in measuring orthogonal velocity components, it requires frequent maintenance and recalibration, which limits its practicality for continuous, large-scale operations. Drifting buoys have also been widely used for measuring near-surface currents. Designed to minimize wind slip, these buoys provide valuable real-time data as they drift with ocean currents, helping researchers track the movement of surface waters across broad areas [4]. The Global Drifter Program (GDP) is an example of a widespread application of this technology, where data collected from drifting buoys have been used in conjunction with satellite data and numerical models to improve ocean current predictions [5]. However, drifting buoys, while effective for long-term monitoring, are affected by wind and wave conditions, which can lead to inaccuracies in estimating pure current velocities. Specifically, wind-induced drift and wave-induced motion can cause the buoys to move in ways that do not accurately reflect the underlying ocean currents, thereby introducing errors in the data collected.

In recent years, the development of remote sensing technologies, particularly radar-based methods, has revolutionized ocean surface current estimation. High-frequency (HF) radar systems have become one of the most widely used remote sensing tools for mapping large-scale surface currents in coastal regions. HF radar measures the Doppler shift of backscattered radio waves to determine current velocity, providing continuous data across a broad spatial range. However, HF radar systems can be sensitive to environmental factors, such as wave orbital motion, which may introduce errors into current estimations [6]. Additionally, HF radar accuracy is often dependent on sea state, with errors ranging from 3 to 10 cm/s under varying wave conditions, which limits its application in rough seas or under heavy wind conditions [7]. While HF radar offers improved spatial coverage compared to ADCPs or drifting buoys, other remote sensing technologies, such as satellite altimeters and Synthetic Aperture Radar (SAR), have also been employed to measure sea surface parameters, including current velocities. Satellite altimeters, for instance, can measure sea surface height and these variations may be used to infer large-scale geostrophic currents, though their application for near-surface current measurement is limited by their coarse spatial resolution [8]. Similarly, SAR provides high-resolution imagery of the ocean surface, which can be used to detect wave patterns and infer current velocities. However, SAR is less effective in regions with high surface roughness or rapidly changing current patterns, limiting its applicability for nearshore environments [9].

X-band marine radar has gained prominence as an effective tool for coastal and nearshore monitoring due to its ability to capture high-resolution images of the sea surface. X-band radar systems offer advantages over traditional methods by providing continuous, large-area coverage with high spatial and temporal resolution, making them well-suited for detecting surface currents, waves, and other oceanographic phenomena. X-band radar has been successfully employed in various coastal monitoring studies, offering valuable data on surface current velocities and wave parameters [10]. However, these radar systems are not without their challenges. X-band radar is particularly sensitive to environmental conditions such as rain and wind. For example, rain can cause scattering and attenuation of the radar signal, which can reduce the accuracy of current estimations [11, 12]. In the field of ocean surface current measurement, X-band radar has demonstrated considerable advantages, but despite significant advancements, there remains ample room for improvement. One of the key benefits of X-band radar is its high spatial and temporal resolution. Typically, X-band radar achieves spatial resolutions of approximately 5-10 meters, depending on system configuration, and temporal resolutions of 1-2 seconds, enabling detailed observations of dynamic ocean surface processes [13]. This high resolution enhances the radar's ability to accurately monitor surface waves and currents, with typical shipborne radar systems effectively covering areas of the ocean surface within a range of 2–5 km. Compared to traditional in-situ instruments, such as ADCPs, X-band radar not only provides current velocity data but can simultaneously capture wave parameters, thus offering a broader scope of oceanographic information [14, 15]. These advancements have greatly expanded the application of X-band radar for coastal monitoring and marine navigation.

However, even with these developments, challenges persist that limit the radar's full potential. One of the ongoing issues is its sensitivity to environmental interference. Rain can cause attenuation and scattering of the radar signal, contributing to noise in the radar returns [16, 17]. Additionally, low sea states result in low backscattering, failing to capture wave signatures on the ocean surface, which leads to unclear radar signals [18]. Moreover, while techniques like Fast Fourier Transform (FFT)-based spectral analysis have been instrumental in extracting frequency and wavenumber information, their effectiveness decreases in complex, non-homogeneous wave fields, such as those near coastlines, where wave patterns are irregular [18]. This highlights a critical need for more advanced noise reduction and signal processing techniques to ensure accurate data extraction.

Recent progress in algorithmic development has addressed some of these challenges. Yet, further refinement is necessary. For example, the local phase gradient method proposed by Wu et al. [18] has shown improvements in regions with complex wave interactions, such as semi-enclosed bays, by enhancing the frequency resolution to provide more accurate current estimations. Similarly, the Polar Current Shell (PCS) method has achieved higher accuracy by transforming radar data into polar coordinates and applying a robust curve-fitting process, particularly in environments characterized by high flow velocities [14]. These improvements have enhanced the radar's utility, but gaps remain in its performance under extreme environmental conditions.

Despite the substantial progress made in utilizing X-band radar for surface current measurement, there remains considerable room for further development. Addressing the radar's susceptibility to environmental noise and improving its ability to handle non-homogeneous wave fields will be key to realizing its full potential. Continued advancements in algorithmic approaches will be crucial for overcoming these limitations and achieving more accurate and reliable surface current measurements.

1.2 Literature Review

X-band radar technology has gained significant traction as a remote sensing tool for monitoring ocean surface currents, offering high-resolution data with spatial resolutions of 5-10 meters and temporal resolutions of 1-2 seconds, enabling detailed observations of dynamic ocean surface processes. These radar systems function by emitting electromagnetic waves, which interact with the ocean surface. The interaction is primarily governed by Bragg resonance, where the radar wavelength resonates with surface gravity waves, causing a strong radar backscatter. This backscatter provides critical information about the ocean surface, such as wave direction, speed, and surface current velocity.

The influence of surface currents on wave patterns is detected through the Doppler effect. As ocean waves propagate in regions with surface currents, their observed frequency shifts, depending on the speed and direction of the current. This shift is crucial for determining surface current velocity and is expressed through the Doppler-shifted wave dispersion relation, which links wave frequency, wavenumber, water depth, and current velocity. The dispersion relation describes how ocean waves behave in the presence of currents, allowing the estimation of surface currents from the radar data by analyzing the frequency shift in the radar signal.

In ideal conditions, the wave frequency observed by the radar is shifted according to the Doppler effect, allowing for relatively straightforward estimation of surface currents. However, deriving accurate current measurements from radar data in real-world environments is more complex. Noise is a major issue for X-band radar systems, arising both from internal system limitations (e.g., electronic noise or hardware imperfections) and external environmental factors such as wind-induced surface roughness, turbulence, and variability in sea state. While the balance between internal and external noise limitations depends on the specific radar design and deployment conditions, in many practical scenarios, external environmental factors dominate the noise profile. This noise can interfere with the radar signal, leading to erroneous estimations. Moreover, ocean environments are rarely homogeneous; coastal areas, in particular, exhibit complex wave fields influenced by local topography, varying water depths, and wind conditions, making it difficult to apply global models to radar data.

1.2.1 Current Estimation Algorithms

Several methods have been developed to tackle the above-mentioned challenges. The Least Squares (LS) curve fitting technique [19] is a widely used method for fitting data to a model by minimizing the sum of the squared differences between observed values and those predicted by the model. In radar-based ocean surface current estimation, the LS technique is applied to adjust the surface current velocity vector to best fit the observed Doppler-shifted wave frequencies to the theoretical wave dispersion relation. The goal is to minimize the discrepancy between the observed and predicted wave frequencies. A key advantage of the LS method is its simplicity and computational efficiency, making it suitable for processing large datasets. It is highly effective when the data quality is high, providing accurate parameter estimates in such cases. Additionally, LS allows for statistical evaluation of the uncertainties in the estimated parameters, offering insight into the confidence of the surface current retrieval. However, the LS technique is sensitive to outliers and noise in the data. Even a few data points that deviate from the expected pattern can have a significant impact on the results, leading to biased or inaccurate current estimates. This is particularly problematic in radar data, which may contain significant noise or spectral aliasing. Spectral aliasing occurs when higher frequency wave components are misrepresented due to insufficient radar sampling, further complicating current retrieval. The LS method assumes a linear relationship between variables, which may not always hold in complex oceanographic environments where nonlinear wave interactions occur. This can reduce the accuracy of the method in such situations. As a result, more advanced techniques, such as Iterative Least Squares (ILS) or Weighted Least Squares (WLS), have been developed to address these limitations by incorporating additional refinements to handle noise, aliasing, and nonlinearity more effectively. In summary, while the LS curve fitting technique is computationally efficient and effective under ideal conditions, its sensitivity to noise, outliers, and aliasing highlights the need for improvements. Enhancements such as noise filtering or iterative approaches could greatly improve its accuracy and reliability in more challenging environments.

The ILS method [20] is an enhanced version of the basic LS technique, designed to improve the accuracy of surface current estimates by iteratively refining the initial parameter estimates. The method works by fitting Doppler-shifted radar data to the wave dispersion relation, starting with an initial estimate of the current velocity. After each iteration, the model is refined by adjusting for nonlinearity in the data and correcting for spectral aliasing. The process continues until the model converges to a stable solution that minimizes the residuals between the observed and theoretical wave frequencies. A significant advantage of the ILS method is its ability to handle complex wave environments and noisy data more effectively than the standard LS method. By iteratively adjusting the parameters, ILS can account for nonlinearities and higher-order harmonics in the wave spectrum, which improves its robustness and accuracy in situations where the wave dynamics are more complex. This makes ILS especially useful in challenging environments, such as low sea states or regions with spectral distortions. However, the ILS method is computationally more intensive than the standard LS technique, as it requires multiple iterations to refine the solution. Its performance also depends heavily on the quality of the initial estimates; poor starting values can slow convergence or lead to less accurate results. Additionally, in very low sea states where wave signals are weak or highly noisy, even ILS may struggle to produce reliable estimates. In summary, while the ILS method offers improved accuracy and robustness over the basic LS approach, especially in complex and noisy environments, it comes with increased computational demands and reliance on good initial estimates. Its effectiveness could be further enhanced by optimizing the iterative process or improving initial estimation techniques.

The WLS (Weighted Least Squares) method [21] is an advanced variation of the Least Squares technique, where each data point is assigned a weight based on its reliability, quantified by factors such as signal strength, noise level, or measurement consistency. In the WLS process, data points with higher reliability (characterized by stronger signal-to-noise ratios or well-defined spectral responses) are given greater weight in the fitting process, while noisier or less certain data points, such as those influenced by weak backscatter, are assigned lower weights to minimize their impact on the final results. This adjustment allows for a more accurate model, especially in situations where some data points may be more affected by noise or distortions. The primary strength of the WLS method is its ability to handle datasets that contain varying levels of uncertainty or noise. By assigning appropriate weights, the method can ensure that outliers or unreliable data do not skew the final results as much as they would in a standard least squares approach. This characteristic makes it particularly well-suited for real-world applications, such as radar-based surface current retrieval, where some portions of the radar data may be of higher quality than others due to environmental conditions or system limitations. However, the effectiveness of WLS heavily depends on having accurate knowledge of the variances or uncertainties of each data point. If the assigned weights are incorrect or poorly estimated, the method may produce biased results, leading to less accurate parameter estimation. Additionally, WLS is more computationally intensive than the standard Least Squares method because it requires the calculation and application of weights for each data point. This added complexity can make it more time-consuming and resource-demanding, especially when working with large datasets. In summary, while the WLS method offers a significant improvement over standard Least Squares by providing a more nuanced approach to data quality, its reliance on accurate weight estimation and the increased computational load are important limitations to consider. It is most effective in situations where data quality varies and where the additional complexity is justified by the need for greater accuracy.

The Dispersive Surface Classificator (DiSC) method [22] is a radar-based remote sensing technique designed to estimate surface currents and bathymetry by analyzing the wave dispersion properties of X-band radar image sequences. This method utilizes the relationship between wave propagation and oceanographic features, such as water depth and surface currents, to create detailed maps of these parameters. By observing the changes in wave patterns caused by variations in bathymetry and currents, the DiSC method can accurately map coastal areas where these factors are highly variable. A major strength of the DiSC method lies in its ability to perform local spectral analysis. Unlike global methods that assume uniform conditions over large areas, DiSC focuses on smaller, localized regions, allowing it to handle inhomogeneous wave fields more effectively. This makes it particularly suitable for analyzing complex coastal environments where wave conditions can change rapidly due to varying bathymetry or obstacles like reefs. Additionally, by decomposing the radar spectrum into different frequency and directional components, the method can better isolate and analyze local wave features, leading to more accurate current and depth estimates. One of the key advantages of the DiSC method is its ability to incorporate higher-order harmonics and correct for aliasing, issues that often degrade the accuracy of radar-based current and depth retrieval methods. By addressing these challenges, DiSC provides more reliable estimates in shallow water environments, where traditional methods relying on deep-water assumptions tend to struggle. However, the DiSC method has limitations. In regions where the waves become highly nonlinear, such as breaking waves or surf zones, the assumptions of linear wave theory used by the method begin to break down. This can lead to inaccuracies, requiring additional corrections for wave steepening and nonlinear dispersion effects. Poor-quality data or insufficient resolution can reduce the effectiveness of the DiSC method, as it relies heavily on the detailed information embedded in the wave spectrum. In summary, the DiSC method is highly effective in shallow and complex coastal regions, offering improved accuracy through local spectral analysis and advanced corrections for aliasing and harmonics. However, its performance can be limited in nonlinear wave environments and requires high-quality radar data for optimal results.

The Normalized Scalar Product (NSP) method [15] is a sophisticated algorithm used for estimating surface currents from X-band radar data. It maximizes the correlation between the radar image spectrum and a characteristic function that represents the dispersion relation of ocean waves, modified by surface currents. The method works by calculating the scalar product between the observed spectrum and the theoretical model of wave propagation. To ensure the results are not affected by variations in signal strength or amplitude, the scalar product is normalized by dividing the scalar product of the filtered image spectrum and the characteristic function by the square root of their total powers. This normalization reduces the influence of noise and makes the NSP method more robust to distortions in the radar data, improving accuracy even in challenging environments. One of the key advantages of the NSP method is its ability to handle noisy data effectively. By normalizing the scalar product, the method reduces the impact of fluctuations in signal strength and aliasing, which can distort current estimates in other techniques like the LS method. This makes NSP particularly useful in high-noise environments or situations where radar spectra may be affected by external distortions like reflections. Furthermore, the use of a characteristic function that accurately represents how surface currents affect wave propagation leads to more reliable estimates of current velocities, particularly in complex ocean conditions. However, the NSP method also has limitations. A major challenge is the requirement for careful tuning of the characteristic function. If this function is not well aligned with the observed radar data, the method may produce inaccurate current estimates. Additionally, the NSP method is computationally intensive compared to simpler methods like LS. The process involves calculating scalar products and normalizing them across multiple frequency and wavenumber components, making it slower and more demanding in terms of computational resources, especially for large datasets or real-time applications. Overall, the NSP method provides a significant improvement in accuracy and noise handling for radar-based surface current estimation, but its effectiveness depends on proper tuning and comes with increased computational complexity.

The PCS method [14] is an advanced algorithm designed for retrieving surface current velocities from X-band marine radar data by transforming radar image spectra into polar coordinates. This method begins by calculating the 3D image spectrum, which contains the wave frequency and wavenumber information, and then extracting the dispersion shell, which represents how wave frequencies are influenced by surface currents. By converting the data from Cartesian to polar coordinates, the PCS method simplifies the process of isolating the effects of surface currents on wave propagation, making it easier to estimate current speed and direction. One of the key steps in the PCS method is the conversion to polar coordinates, which restructures the data to focus on the wave frequency shifts caused by surface currents. This transformation helps isolate the radial and angular components of the wave frequency, making the subsequent curve fitting process more efficient and accurate. By fitting sinusoidal curves to the data, the method estimates the current velocity and direction with high precision. Additionally, the PCS method includes noise reduction and outlier removal processes to ensure that anomalies in the radar data do not affect the final estimates. The main advantages of the PCS method are its robustness and computational efficiency. The transformation to polar coordinates streamlines the curve-fitting process by isolating variables, organizing data along radial and angular elements, reducing noise, and improving the accuracy and efficiency of the fit. The PCS method is also computationally efficient, making it suitable for real-time applications where quick and reliable surface current estimates are needed. This makes it highly useful in operational marine environments. However, the PCS method has some limitations. It assumes deep-water conditions, which restricts its effectiveness in shallow coastal areas where the wave dispersion relation is more complex. Additionally, the accuracy of the method depends on the precise extraction of the dispersion shell, which can be difficult in low sea states or highly noisy environments. In such cases, the performance of the PCS method may degrade. Future improvements could focus on extending the method's applicability to shallow water environments and enhancing its robustness against noise and incomplete data. Overall, the PCS method is a powerful tool for surface current estimation, offering significant advantages in terms of accuracy and efficiency, but it requires further adaptation to handle more complex environments and noisy conditions.

The Cross-Spectral Correlation (CSC) [23] approach is a method used to estimate surface currents by analyzing the coherence and phase relationships between sequential X-band radar images of the ocean surface. By examining the correlation between pairs of radar images, the CSC approach measures the phase velocity of ocean waves and relates it to the surface current velocity through the Doppler effect. This method is particularly well-suited for use in noisy environments and in areas with inhomogeneous wave fields, such as nearshore regions, where traditional methods may struggle to provide accurate results. The process begins with preprocessing the radar images to enhance wave patterns and make the radar backscatter uniform across the image. This step ensures better accuracy in the subsequent current velocity retrieval. The cross-spectrum between neighboring radar images is then calculated to identify how wave patterns change over time. The coherence, which measures the strength of the correlation between images, is used to filter out unreliable data, while the phase relationship provides information on the wave propagation speed. By focusing on wave components with high coherence, the CSC method ensures that only the most reliable wave data are used for current estimation. The primary advantage of the CSC method is its robustness in noisy environments. By focusing on the cross-spectral coherence and phase, it reduces the influence of noise, reflections, and other distortions that can degrade the quality of radar data. This makes the method particularly effective in nearshore regions or areas with complex wave fields, where other approaches may struggle. The CSC method also performs well when dealing with inhomogeneous wave fields, as it can extract reliable current estimates even when wave conditions vary across the radar image. However, the CSC method has some limitations. It requires careful preprocessing and filtering of radar data to ensure that only coherent wave components are used for current estimation. Without proper filtering, noise or low-coherence components could introduce errors. Additionally, the method assumes a linear wave dispersion relation, which may not be valid in shallow water environments or in areas with strong nonlinear wave interactions. In such cases, the CSC approach may produce less accurate results, as the underlying assumptions about wave behavior become less reliable. In summary, the CSC method offers a robust approach to surface current estimation, especially in complex and noisy environments. Its ability to filter out unreliable data and focus on coherent wave components improves accuracy, but its reliance on preprocessing and the assumption of linear wave behavior can introduce limitations in certain conditions.

In a recent study by Wu et al. [18], the local phase gradient-based method is employed to effectively estimate spatial currents despite the complex circulation patterns inherent to bay areas. The method is based on the local phase gradient technique, which estimates the spatial wavenumber of ocean waves from radar images to determine the surface current. Unlike traditional methods that rely on global spectral analysis, the local phase gradient method allows for higher spatial resolution and better handling of inhomogeneous conditions often present in semi-enclosed bays. The local phase gradient method improves the accuracy of surface current estimations by applying bandpass and directional filtering to radar image sequences, isolating specific wave components that are used to calculate wavenumbers. These wavenumbers are then analyzed to estimate the current velocity. The method is particularly effective in reducing the influence of noise and non-wave components in the radar data, which can distort current estimations. One of the key strengths of this method is its ability to resolve spatially variable currents in complex coastal environments, such as semi-enclosed bays, where traditional methods struggle due to the inhomogeneity of the current field. The technique is also robust in capturing smaller-scale features like eddies, which are often present in coastal areas. However, the method has limitations, particularly in low-current environments where the radar may struggle to detect weak surface currents, and the computational complexity can be higher due to the need for localized analysis. In summary, this new method provides a more reliable and spatially detailed way to estimate surface currents in semi-enclosed bays, addressing many of the shortcomings of traditional techniques, especially in handling complex and inhomogeneous coastal environments. The main trade-offs are the increased computational demand and challenges in detecting very weak currents.

1.2.2 Factors Affecting the Accuracy of Surface Current Measurements

Several factors significantly impact the accuracy of radar-based surface current measurements, including vessel motion and precipitation. Vessel movement, particularly Doppler shifts and spatial misalignments caused by ship motion, introduces errors in georeferencing radar images and measuring current velocities. Traditional radar processing methods assume a stationary platform, and when applied to moving vessels, they result in inaccuracies.

For instance, a vessel travelling at 6 m/s can cause mapping errors of up to 10 meters during a single antenna rotation, and even heading changes as small as 1° can lead to errors up to 70 meters at longer ranges [24, 25]. These errors are further compounded by significant changes in ship speed and heading during radar sweeps, leading to spatiotemporal aliasing that distorts ocean wave frequencies and wavelengths [26].

To mitigate these effects, georeferencing techniques correct radar data by accounting for the vessel's position, speed, and heading during acquisition, transforming the radar images into a fixed spatial grid. Advanced compensation methods, such as multiantenna GPS systems combined with high-precision gyrocompasses, further correct for heading biases and vessel-induced distortions, maintaining surface current estimation accuracy even at significant vessel speeds [25, 26]. In cases where Doppler shifts caused by vessel motion are significant, corrections must be applied to observed wave frequencies to address distortions in the wave spectrum [27], and time-domain spectral filtering techniques are used to remove spurious signals from vessel motion, improving the reliability of current estimations [27].

Additionally, precipitation introduces noise into radar signals, further complicating surface current estimations. Rain contamination significantly degrades the accuracy of algorithms such as PCS and NSP, increasing errors in current speed and direction measurements. Under rain-contaminated conditions, correlation coefficients (CCs) for speed and direction dropped to 0.57 and 0.65, respectively, compared to 0.73 and 0.91 in rain-free conditions. Root mean square deviation (RMSD) values also increased from 0.12 m/s to 0.20 m/s for speed and from 25.1° to 58.1° for direction under rain [28]. Despite advancements in algorithm development and compensation techniques, vessel motion and precipitation remain significant challenges for achieving accurate surface current measurements.

1.3 Objectives

The primary goal of this research is to improve the accuracy and robustness of ocean surface current estimation using X-band radar systems by developing an enhanced algorithm based on the PCS method. This study seeks to address existing challenges, including noise, spectral aliasing, and localized errors, by integrating advanced noise filtering techniques, implementing a unified curve-fitting approach, and enhancing algorithmic robustness against environmental distortions.

A key aspect of this research is the incorporation of sophisticated noise filtering techniques, such as Kernel Density Estimation (KDE) and Interquartile Range (IQR) filtering, to improve data quality under calm sea conditions where traditional PCS methods struggle. These filters will effectively detect and remove noise and outliers, enabling more precise surface current estimates. To further enhance algorithmic efficiency, the research introduces a unified curve-fitting process that replaces the PCS method's segmented fitting for different radial wavenumbers. This unified approach reduces computational complexity and ensures consistent and accurate results across the entire radar spectrum. Additionally, the research addresses spectral aliasing and distortions caused by environmental factors such as inhomogeneous wave fields. By incorporating spectral refolding techniques and accounting for higher harmonic components, the algorithm aims to deliver more reliable current estimates, even in complex wave conditions.

The effectiveness of these improvements will be validated using both simulated and real-world radar datasets. Simulated data will provide controlled testing environments for evaluating algorithm performance under various conditions, while real-world datasets will demonstrate its applicability in dynamic operational scenarios. Finally, the enhanced PCS algorithm will be compared against the original PCS method and other radar-based techniques, evaluating improvements in accuracy, computational efficiency, and robustness to environmental factors. This comprehensive assessment will highlight the practical advantages of the proposed method for diverse maritime applications.

1.4 Research Scope and Outline

This thesis presents a novel algorithm for surface current retrieval, focusing on improving data reliability and accuracy. The research encompasses both theoretical development and practical validation through radar data analysis.

The structure of the thesis is as follows: Chapter 2 introduces a newly developed, simple symmetry-based algorithm and demonstrates its application to simulated radar data for validation purposes. Chapter 3 builds on this symmetry-based algorithm, combining it with the PCS method to develop a new hybrid algorithm, which is applied to both simulated and real-world radar data for evaluation. Finally, Chapter 4 presents the conclusions and recommendations for future research.

The achievements of this research have been published in the following papers:

1. Y. Li and W. Huang, “An algorithm for ocean current inversion from X-band marine radar images”, in *Proc. 2024 IEEE Intl. Geosci. Remote Sens. Symp. (IGARSS)*, Athens, Greece, 7-12 July 2024, pp. 5956–5960.

2. Y. Li, Z. Yang, and W. Huang, “Improved polar current shell algorithm for ocean current retrieval from X-band radar data”, *Remote Sens.*, vol. 16, no. 22, 2024, Art. no. 4140.

Chapter 2

An Algorithm for Ocean Current Inversion from X-band Marine Radar Images

2.1 Abstract

An algorithm for extracting sea surface current information from X-band nautical radar image sequences is presented in this paper. The angular frequencies corresponding to the wave numbers are first extracted from the radar image sequence, and then the Doppler shifts corresponding to every wave numbers are calculated. The Doppler shifts corresponding to wave vectors symmetric with respect to the origin of the wave number plane are used to estimate current speed and direction. The test using simulated data shows that the RMSD of the current speed is 0.13 m/s and that of the current direction is 1.4°. The results

---

This chapter has been published in IEEE International Symposium on Geoscience and Remote Sensing (IGARSS). The full text of the published paper is available to read at this link: https://ieeexplore.ieee.org/document/10641988.

Author Contributions: All authors made substantial contributions to the conception and the design of the study. Y.L. performed the experiments, analyzed the data and wrote the paper. W.H. reviewed, edited, and revised the paper. All authors reviewed and commented on the manuscript.

illustrate that the method is feasible with accuracy comparable to existing methods.

2.2 Introduction

The measurement of ocean currents is crucial for understanding global climate dynamics, sustaining marine ecosystems, aiding maritime navigation and conducting scientific research. Additionally, accurate current information is important for ocean wave parameter estimation, such as significant wave height [29–32]. Over the last few decades, X-band radar has become a prominent tool in ocean surface current measurement, offering high-resolution, real-time data crucial for in-depth and dynamic coastal studies. It scans the ocean surface through microwave interaction with sea waves [33, 34].

X-band radar image sequences are instrumental in deducing ocean surface current speed and direction. Several methodologies have been developed to estimate surface currents. Young et al. [19] utilized an LS curve fitting technique to determine ocean currents that influence wave frequency changes. The ILS approach [20] enhanced the LS method by introducing an iterative approach, updating the current speed over a fixed number of iterations, guided by the higher order harmonic dispersion relation. Gangeskar [21] first introduced an algorithm to enhance traditional methods by correcting key error sources. The DiSC method [22] is a technique that merges directional dispersion frequency filters with the basic principles of the least squares method. The NSP [15] procedure estimates surface current vectors by maximizing the scalar product. The PCS [14] algorithm, on the other hand, transforms dispersion shells from Cartesian to polar coordinates and estimates current speed and direction based on the relationship between the wavevector and the current velocity through curve fitting.

Despite significant advancements in the field of ocean current estimation techniques, critical challenges persist. A primary limitation lies in verifying the accuracy of the extracted dispersion shells, a crucial step for the reliable estimation of ocean currents. This gap undermines the accuracy and efficiency of current estimation. This paper aims to address this critical gap by introducing a novel algorithm that significantly enhances the reliability of data points extracted from the dispersion shell. By leveraging the symmetry of Doppler shifts (SDS) to eliminate data tainted with noise before beginning iterative calculations, this approach retains only the most reliable data for ocean current estimation. The paper is organized as follows: Section 2.3 describes the methodology and principles of the proposed algorithm. Section 2.4 shows the results of the method on simulated data. Section 2.5 summarizes the findings and suggests future research directions.

2.3 Methodology

2.3.1 Obtaining 3D Image Spectrum

The first step is to obtain a sequence of sub-regions ($m \times n \times t$) from original radar images, where m indicates the number of pixels along the height of the sub-region, n indicates the number of pixels along the width, and t specifies the number of images in the sequence, i.e., the temporal dimension of the dataset. To mitigate background noise and enhance the contrast, the mean intensity value is deducted from the pixel intensities within each sub-region. A tapering function proposed by Shen et al. [14] is then applied to ameliorate the Gibbs phenomenon. To augment the frequency resolution, zero-padding is employed to expand the data dimension to $256 \times 256 \times 256$. Finally, by squaring the spectral amplitude derived from the three-dimensional (3D) FFT, the power spectrum $P_0(k_x, k_y, \omega)$ is obtained.

2.3.2 Extracting the Dispersion Shell

To remove the static component, a high-pass filter is applied to obtain the filtered energy spectrum $P_1(k_x, k_y, \omega)$.

$$P_1(k_x, k_y, \omega) = \begin{cases} 0, & \omega < \overline{\omega} \\ P_0(k_x, k_y, \omega), & \omega \geq \overline{\omega}, \end{cases} \tag{2.1}$$

where the cut-off frequency is empirically taken as $\overline{\omega} = 0.03 \cdot 2\pi$ radian/s [35].

For a wave vector $\vec{k}(k_x, k_y)$ in the wavenumber plane, the spectral energy at ω_i is denoted as $P_i(k_x, k_y, \omega_i)$. The peak energy frequency ω_k corresponds to the maximum energy P_{max} among all $P(k_x, k_y, \omega_i), (1 \leq i \leq 256)$. Combining the peak energy points of each wave vector forms the dispersion shell $\omega(k_x, k_y)$.

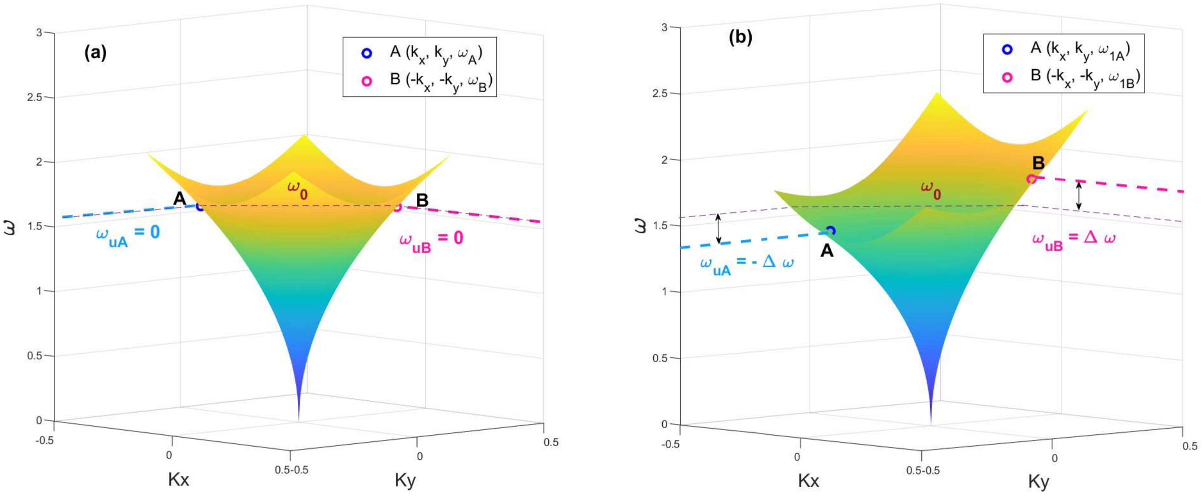

Figure 2.1: (a) Intrinsic and (b) Doppler-shifted dispersion shells in the (k_x, k_y, ω) domain. A and B are two spectral points for two wavevectors symmetric about the origin of the wave number plane, and their angular frequencies are shown to be the same in (a), which are both ω_0. In (b), the Doppler shift of A is ω_{u_A}, the Doppler shift of B is ω_{u_B}, and $\omega_{u_A} + \omega_{u_B} = 0$.

2.3.3 Identifying Stable Points

1. **Determining the Doppler Shift**

   In the absence of surface current, the angular frequency ω_0 of the wave is given by

$$\omega_0 = \sqrt{g|\vec{k}| \tanh(|\vec{k}|d)}, \tag{2.2}$$

   where g represents the acceleration due to gravity, $\vec{k}$ denotes the wavevector, d stands for the water depth. In the assumption of sufficiently deep water, the equation can be simplified to

$$\omega_{0_k} = \sqrt{g|\vec{k}|}. \tag{2.3}$$

An acceptable cutoff for the hyperbolic tangent's argument under the sufficiently deep water assumption typically satisfies

$$|\vec{k}|d \gg 1, \tag{2.4}$$

so the $\tanh(|\vec{k}|d)$ can be considered as 1. An intrinsic dispersion shell for deep water is shown in Fig. 2.1 (a). When a surface current $\vec{U}$ is present, the angular wave frequency ω_1 can be expressed as

$$\omega_1 = \sqrt{g|\vec{k}|} + \vec{k} \cdot \vec{U}. \tag{2.5}$$

The corresponding Doppler-shifted dispersion shell is depicted in Fig. 2.1 (b). The Doppler shift caused by current $\vec{U}$ is

$$\omega_u = \omega_1 - \omega_0 = \vec{k} \cdot \vec{U} = k_x U_x + k_y U_y. \tag{2.6}$$

After obtaining the dispersion shell $\omega_1(k_x, k_y)$ from the radar sub-images, the intrinsic frequency ω_{0_k} of every wavevector is subtracted from ω_1 to acquire $\omega_u(k_x, k_y)$.

Fig. 2.2 is an example showing the Doppler shifts for some origin-symmetric wavevector pairs extracted from a simulated file with a current speed of 2 m/s and a direction of 180° at low noise levels. The low noise levels here refer to the wave vector pairs where the difference in Doppler shift frequency amplitudes is minimal.

2. **Symmetry in Doppler Shift**

The Doppler shift corresponding to $\vec{k}(k_x, k_y)$ is

$$\omega_{u_k} = \vec{k} \cdot \vec{U} = k_x U_x + k_y U_y. \tag{2.7}$$

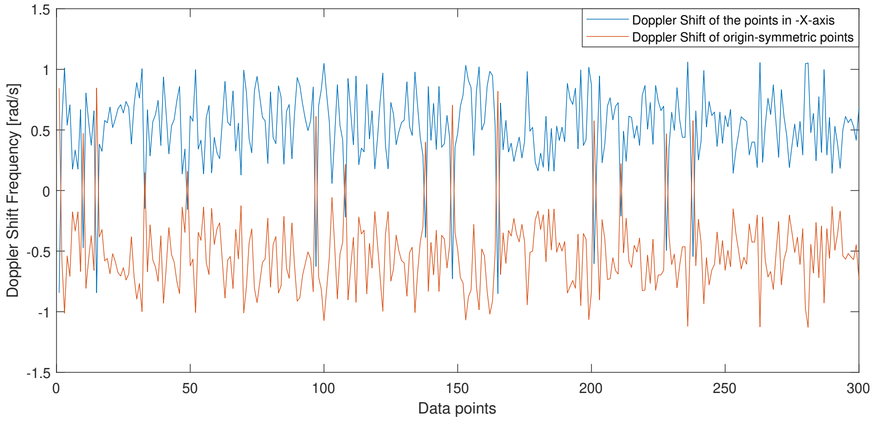

Figure 2.2: The Doppler shift of origin-symmetric points in the wave number plane

The Doppler shift for $k'(-k_x, -k_y)$, which is symmetric to $k(k_x, k_y)$ with respect to the origin of the wavenumber plane, is

$$\omega_{u_{k'}} = \vec{k'} \cdot \vec{U} = -k_x U_x - k_y U_y. \tag{2.8}$$

The sum of the Doppler shifts for these two symmetric wavevectors should be zero, i.e.,

$$S_{\omega(k,k')} = \omega_{u_k} + \omega_{u_{k'}} = 0. \tag{2.9}$$

Next, a process for selecting the wave vectors with low noise and error is implemented as

$$\omega_{\text{filt}}(k_x, k_y) = \begin{cases} \omega_k & \text{if } E_{\omega_u} \leq E, \\ \text{NaN} & \text{otherwise} \end{cases} \tag{2.10}$$

where E_{ω_u} is the symmetric wavevector Doppler shift mean absolute deviation (MAD) ratio and can be expressed as

$$E_{\omega_u} = \frac{|S_{\omega(k,k')}|}{\frac{1}{2}\left(|\omega_{u_k}| + |\omega_{u_{k'}}|\right)}, \tag{2.11}$$

Here, NaN stands for "Not a Number" and is used to indicate that the value is undefined or unrepresentable. In this context, NaN is used to mark values that should be deleted or ignored in subsequent analysis because they do not meet the required threshold. The threshold E is chosen to be 0.1. The value of 0.1 is selected based on empirical observations and prior studies indicating that this threshold effectively balances the trade-off between noise reduction and error minimization.

2.3.4 Estimating the Current Parameters

High-quality points (k_x, k_y, ω_u) are identified in accordance with the criteria outlined above. The particular parameter values are chosen based on empirical observations and prior studies that indicate their effectiveness in minimizing errors and streamlining further iterations. Typically, only the 20 point pairs with the lowest E_{ω_u} values are chosen. So far, we have obtained a collection of 20 pairs of linear equations as given by (2.7) and (2.8). For each pair, the corresponding wavevectors are exactly in opposite directions, while the Doppler shift values are nearly opposites due to the presence of different error sources. Therefore, to minimize redundancy, our attention is centred on the 20 equations derived from the wavevectors in the half-plane $k_x < 0$ within the (k_x, k_y, ω) domain. Upon pairwise solving the set of 20 equations, we obtain a total of 190 solutions, denoted as $S = \{(U_{x_i}, U_{y_i})\}_{i=1}^{190}$. The selection of these equations based on the symmetry in the Doppler shift guarantees that these estimates for U_x and U_y are concentrated around their actual values.

At this point, a few outliers may exist due to the fact that both of the extracted pairs contain large errors but their Doppler shifts sum is close to 0. This is less common but it needs to be eliminated. The K-means clustering algorithm [36] is used to exclude these outliers. A histogram is generated for the set of remaining estimated values to identify the bin that exhibits the highest occurrence of data points, which will serve as an initial approximation of the most densely populated interval. After this, the methodology involves constructing a refined histogram by adjusting the bin width within the bounds of this initially identified interval, again focusing on the bin with the peak occurrence of data points. This refinement process is conducted iteratively, progressively narrowing the bin width until the width of the most densely populated interval is 0.5 or less. This specific width criterion is chosen for its balance between accuracy and inclusivity, as determined through prior experimentation with datasets of similar characteristics. On the one hand, a larger interval might encompass a significant number of outliers, potentially skewing subsequent iterations and affecting the precision of the analysis. On the other hand, an excessively narrow interval could lead to the exclusion of genuine data points, especially in the presence of minor errors. Therefore, a width of 0.5 strikes an optimal balance, minimizing the impact of outliers while ensuring that true data values are retained within the analysis scope. While this threshold is not entirely dataset-independent, it has been validated across datasets with similar distributions and characteristics, ensuring its generalizability within the scope of this study.

Once the final estimation range is determined, only those equations yielding solutions that fall within this acceptable interval are retained. Finally, a least squares method is applied to the remaining points to obtain the final optimal U_x and U_y.

2.4 Simulation Results

The study utilizes a variant of the Pierson-Moskowitz (PM) [37,38] ocean spectrum combined with a cardioid directional function [39] to simulate ocean surface. The PM model describes the wave spectrum of a fully developed sea. Introduced by Pierson and Moskowitz in 1964 [37], it assumes waves have reached a steady state under an infinitely long wind field. The PM model's wave spectrum formula is

$$S(f) = \alpha g^2 (2\pi)^{-4} f^{-5} \exp\left(-\frac{5}{4}\left(\frac{f_p}{f}\right)^4\right) \tag{2.12}$$

where $S(f)$ is the spectral density at frequency f, α is an empirical constant (0.0081), g is the gravitational acceleration (9.81 $\mathrm{m/s^2}$), f is the wave frequency, and f_p is the peak frequency. The directional spreading function $D(\omega, \theta)$ is given by [40]

$$D(\omega, \theta) = \frac{2^{s-1}\Gamma^2(s+1)}{\pi\Gamma(2s+1)} \cos^{2s}\left(\frac{\theta - \bar{\theta}}{2}\right) \tag{2.13}$$

where ω is the angular frequency, θ is the azimuth angle, $\bar{\theta}$ is the mean wave direction, s is a parameter that controls the angular spreading and is a function of the wave frequency, and Γ is the Gamma function. The parameter s is defined as

$$s(f) = s_{\max}\left(\frac{f}{f_p}\right)^{\mu} \tag{2.14}$$

where f is the wave frequency, f_p is the peak wave frequency, $s_{\max}$ is the maximum value of s, μ is a parameter that has different values depending on the wave frequency

$$\mu = \begin{cases} 5, & \text{when } f \leq f_p \\ -2.5, & \text{when } f > f_p \end{cases} \tag{2.15}$$

This combination forms the ocean wave power spectrum, which is expressed as the product of a non-directional wave spectrum (the PM spectrum) and a directional factor (the cardioid function). This approach allows for the generation of a realistic ocean surface with irregular waves, accounting for both the frequency characteristics and the directional properties of the waves. This simulation generates sets of data corresponding to various scenarios of ocean currents, facilitating the comparison of the proposed method with two existing algorithms: the PCS and NSP methods. In total, there are 89 simulated image sequences corresponding to four sets: 1) current speed varies from 0.5 to 10 m/s with current direction 150°; 2) current speed changes from 0.5 to 10 m/s with current direction 180°; 3) current speed is 6-15 m/s with current direction 150°; 4) current speed is 0.5-15 m/s with current direction 150°. In this study, all current directions are measured clockwise from true

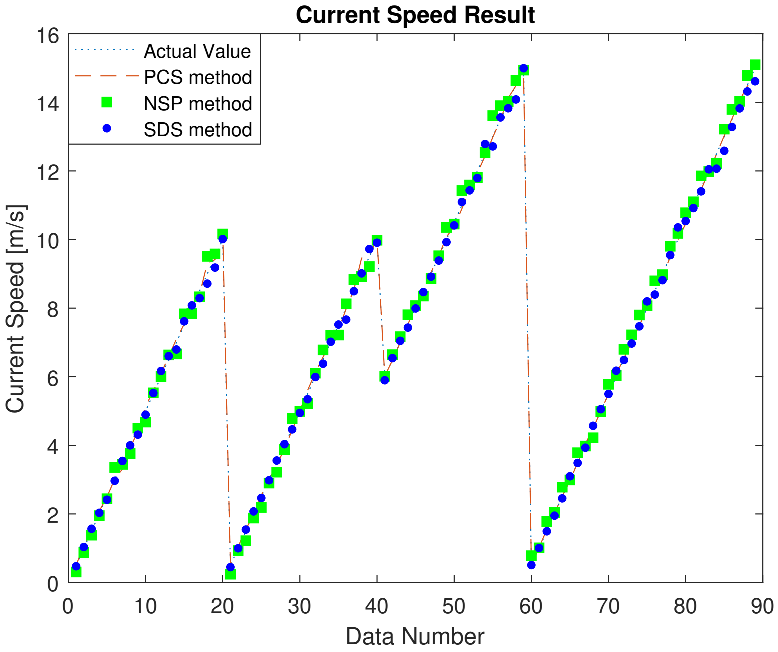

Figure 2.3: Current speed comparison

north. These simulated data allow for the testing of the algorithm's accuracy and robustness when estimating currents of different directions. A direction of 150° represents a relatively common scenario where the current direction differs from the wave direction, whereas 180° signifies a special case, where the current is in the same direction as the wave. Testing both scenarios ensures that the algorithm can perform reliably under various conditions. The comparative analysis is depicted in Figs. 2.3 and 2.4, and Table 2.1.

As far as current speed is concerned, the RMSDs of the PCS, SDS and NSP methods are 0.10 m/s, 0.13 m/s, 0.22 m/s respectively. The results of the PCS method and SDS are close to each other, i.e., around 0.1 m/s, while that of the NSP has a relatively larger error (over 0.2 m/s). For current direction, the RMSDs of the PCS, SDS and NSP methods are 1.2°, 1.4° and 3.8°, respectively. The results of PCS and SDS are both less than 1.5°, while that of NSP is more than 3.5°.

The results reveal the proposed method's effectiveness in estimating ocean current speed and direction. Notably, the RMSD values indicate that the proposed method generally

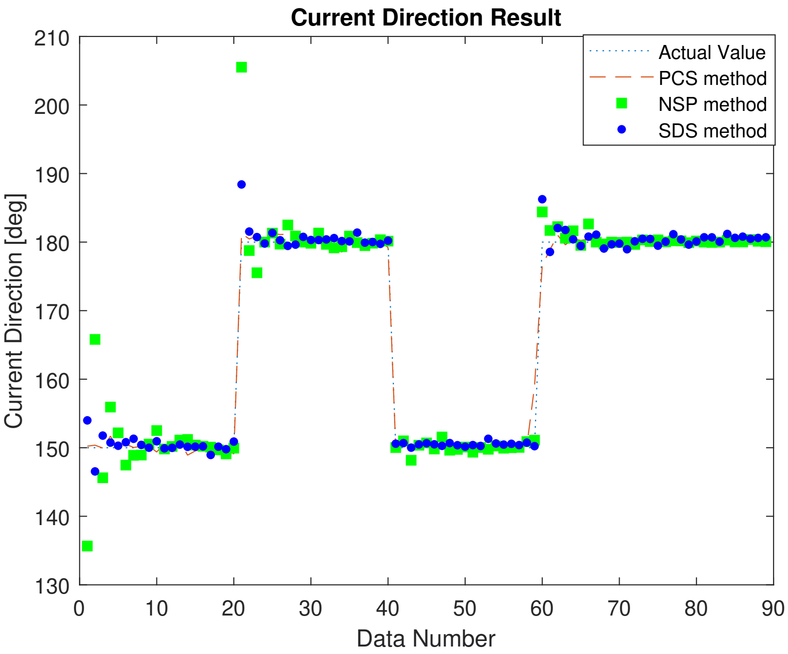

Figure 2.4: Current direction comparison

achieves some more accurate current estimates than the NSP method. Although the PCS method demonstrates a slightly higher accuracy, the difference in performance is marginal.

To further assess the efficacy of the SDS method, we selected the wavevectors from the half-plane $k_x < 0$ in the (k_x, k_y, ω) domain. Our focus was to investigate the dependence of the Doppler shift error of the wavevectors, derived from subtracting the measured Doppler shift from the true Doppler shift, on the Doppler shift MAD ratio E_{ω_u}. The results are presented in Fig. 2.5. Observing the overall trend, it is evident that as the value of E_{ω_u}

Table 2.1: Error analysis

Method	**Current speed**		**Current direction [deg]**
	RMSD [m/s]	**Root Mean Square Percentage Error RMSPE**	**RMSD**
PCS	0.10	0.1%	1.2
SDS	0.13	0.3%	1.4
NSP	0.22	0.8%	3.8

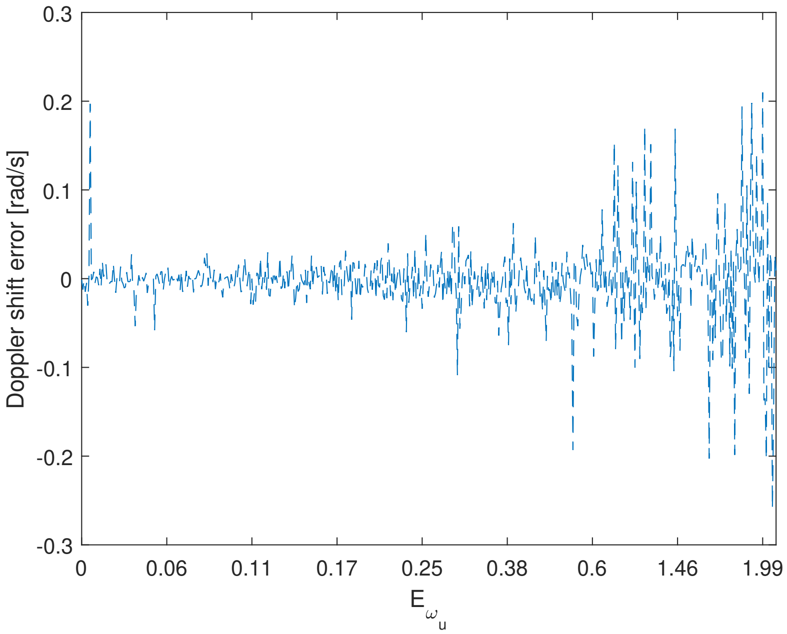

Figure 2.5: The dependence of the Doppler shift error on E_{ω_u} of the wavevectors from the half-plane $k_x < 0$ in the (k_x, k_y, ω) domain.

increases, there is a corresponding increase in the Doppler shift error.

2.5 Chapter Summary

In this chapter, a new method that utilizes the symmetry of the Doppler shifts induced by ocean currents is proposed for current estimation. Application of this methodology to simulated radar images, which include added noise, showed its effectiveness in extracting surface current speed and direction. The SDS method embeds a valuable filtering and validation mechanism, capable of minimizing anomalies when extracting the angular frequency associated with each wave number vector. This ensures that high-quality spectrum points are selected for subsequent analysis.

It is important to acknowledge that the absence of symmetrical wavenumber shift data could potentially compromise the full exploitation of the wavenumber plane's symmetry. However, this limitation does not render the analysis futile. Currently, the methodology has been validated only against simulated radar data. Future work will involve applying this method to actual radar observations and assessing the viability of this approach to strengthen the veracity of our findings.

Chapter 3

Improved Polar Current Shell Algorithm for Ocean Current Retrieval From X-Band Radar Data

3.1 Abstract

This paper presents an improved algorithm for retrieving ocean surface currents from X-band marine radar images. The original Polar Current Shell (PCS) method begins with a 3D fast FFT of the radar image sequence, followed by the extraction of the dispersion shell from the 3D image spectrum, which is then transformed into a PCS using polar coordinates. Building on this foundation, the improved approach is to analyze all data points

---

This chapter has been published in Remote Sensing. The full text of the published paper is available to read at this link: https://www.mdpi.com/2072-4292/16/22/4140.

Author Contributions: All authors made substantial contributions to the conception and the design of the study. Y.L. performed the experiments, analyzed the data and wrote the paper. Z.Y. and W.H. reviewed, edited, and revised the paper. All authors reviewed and commented on the manuscript.

corresponding to different wavenumber magnitudes in the PCS domain rather than analyzing each specific wavenumber magnitude separately. In addition, Kernel Density Estimation (KDE) to identify high-density directions, interquartile range filtering to remove outliers, and symmetry-based filtering to further reduce noise by comparing data from opposite directions are also utilized for further improvement. Finally, a single curve fitting is applied to the filtered data rather than conducting multiple curve fittings as in the original method. The algorithm is validated using simulated data and real radar data, including the data collected by a Decca radar in 2008 and that by a Koden radar in 2017. For the 2008 Decca radar data, the improved PCS method reduced the RMSD for speed estimation by 0.06 m/s and for direction estimation by 3.8° while improving the correlation coefficients (CCs) for current speed by 0.06 and direction by 0.07 compared to the original PCS method. For the 2017 Koden radar data, the improved PCS method reduced the RMSD for speed by 0.02 m/s and for direction by 4.6°, with CCs being improved for current speed by 0.03 and direction by 0.05 compared to the original PCS method.

3.2 Introduction

The retrieval of ocean surface currents plays a crucial role in a variety of marine applications, including navigation, coastal monitoring, Search-and-Rescue (SR) missions, oil spill response, and marine debris tracking [10,41]. Traditional methods for measuring ocean surface currents, such as drifting buoys [4,5], ADCPs [2,42], and current meters [3], although useful for providing localized current data, have significant limitations. These methods are often costly to deploy, complex to maintain, limited in spatial coverage, and challenging to operate continuously in harsh marine environments. The data they collect are typically point-based, which fail to capture the broader dynamics of ocean currents over large areas [1]. With advancements in technology, remote sensing offers the capability to provide large-scale, real-time, and continuous surface current data, allowing researchers to gather comprehensive flow information without direct contact with the ocean [19]. This significantly enhances the efficiency and spatial coverage of data acquisition [43]. Several types of sensors, such as HF radars [6, 7, 44], X-band marine radars [15], satellite altimeters [8], and SAR [9], have commonly been used in remote sensing to measure ocean surface currents in recent years. Compared to other remote sensing sensors, X-band radars hold significant advantages when monitoring ocean surfaces within a range of several kilometres [11]. Their high spatial and temporal resolution allows for the precise tracking of small-scale current [45], wind [12, 46], and wave dynamics [30–32, 47]. The ease of deployment, lower maintenance requirements, and cost-effectiveness of X-band radars further enhance their practicality for ocean surface measurements [27].

When an X-band radar transmits electromagnetic waves, they interact with the ocean surface waves that match the Bragg scattering condition, where the radar wavelength is twice that of the ocean waves. This scattering mechanism amplifies the backscatter signal, which can provide detailed information about the sea surface. It is found that the motion of the surface waves influenced by currents will cause an extra Doppler shift in the frequency of the backscattered signals [19]. Based on this principle, several algorithms have been developed for retrieving ocean currents from X-band radar data. Traditional approaches include the LS curve-fitting technique [19], the ILS approach [20], the WLS method [21], the DiSC method [22], and the NSP procedure [15]. A more recent development is the PCS method [14], which transforms radar image spectra into polar coordinates for surface current retrieval. This method offers a robust alternative to previous approaches by providing a more structured framework for current estimation. Dual-polarized radar systems have also been shown to improve current retrieval accuracy, with certain sea state conditions benefiting from vertical polarization [48]. Chen et al. [23] demonstrated an improved cross-spectral correlation approach for deriving sea surface currents from X-band marine radar images, providing another robust method comparable to traditional FFT-based methods. In a recent study by Wu et al. [18], the local phase gradient-based method is employed to effectively estimate spatial currents despite the complex circulation patterns inherent to bay areas. Moreover, Wang et al. [49] demonstrated the application of machine learning algorithms, including linear regression and neural networks, to enhance the estimation of surface current from radar data. With the maturation of technology, X-band marine radars have also developed several commercial applications for current measurements, such as Wave Monitoring System II (WaMoS II) [50]. This system provides real-time, high-resolution current data under various weather conditions and is widely used in marine engineering. For instance, Derkani et al. [51] utilized WaMoS II during the Antarctic Circumnavigation Expedition to collect wave spectra and surface current data, applying calibration methods to improve data accuracy and validating the results with satellite observations.

Despite these advancements, challenges remain in current retrieval, especially when dealing with noisy datasets or outliers that can degrade the accuracy of the results. In low-sea-state conditions, traditional radar methods (e.g., ILS and NSP) struggle due to the lower signal-to-noise ratios of radar backscatter from calm sea surfaces, as noted by Huang et al. [52]. The original PCS method, while robust in many scenarios, can produce inaccurate results when the number of valid data points for curve fitting is insufficient or when noise is prevalent. Moreover, inaccurate current estimation may affect subsequent wave parameter estimations [29,40]. This limitation underscores the necessity for an improved PCS algorithm that addresses these issues. In response, this paper introduces an improved PCS algorithm with several key enhancements. The improved algorithm incorporates an outlier rejection process to filter noise before curve fitting, as well as a unified fitting method that considers the entire dataset collectively, reducing localized errors. Symmetry-based noise filtering is also introduced according to the symmetry of Doppler-shifted dispersion shells, further refining the results. These improvements have been validated using both simulated and real radar data, showing significant gains in accuracy without adding to the computational complexity.

The structure of this paper is as follows: Section 3.3 details the original PCS method, followed by Section 3.4, which presents the specific improvements made to the PCS algorithm. Section 3.5 provides performance validation through simulations and real-world radar data. Finally, Section 3.6 concludes with recommendations for further research and potential future improvements.

3.3 The PCS Current Algorithm

The PCS algorithm [14] provides an efficient approach for estimating ocean surface currents using X-band marine radar data by transforming radar image spectra into polar coordinates. The detailed current retrieval processes are described as follows.

3.3.1 Image Spectrum Generation

The process starts by selecting a sequence of sub-regions ($I \in \mathbb{R}^{m \times n \times t}$) from the original radar images, where m indicates the number of pixels along the height of the sub-region, n indicates the number of pixels along the width, and t is the number of images in the sequence, representing the temporal dimension. In this work, m, n, and t are equal to 128, 128, and 32. To enhance contrast and minimize background noise, the mean intensity of each sub-region is subtracted from the pixel values. Next, to reduce the Gibbs phenomenon, a tapering function is applied. The frequency resolution is then improved by applying zero-padding, expanding the data dimensions to $256 \times 256 \times 256$. This zero-padding size was chosen based on balancing the computational load spectral resolution. The power spectrum, $P_0(k_x, k_y, \omega)$, is finally derived by squaring the spectral amplitude obtained from the 3D FFT.

3.3.2 Dispersion Shell Identification

The dispersion shell is identified based on the linear (fundamental) wave dispersion relationship, assuming deep water conditions. The dispersion relation, including the effect of ocean currents, is given by

$$\omega = \sqrt{gk} + \vec{k} \cdot \vec{U} \tag{3.1}$$

where ω is the angular frequency, which includes the Doppler shift from the current, g is the gravitational acceleration, $k = \sqrt{k_x^2 + k_y^2}$ is the wavenumber, $\vec{U}$ is the surface current velocity vector, and $\vec{k} \cdot \vec{U} = kU\cos(\theta)$ is the Doppler shift caused by the ocean current, with θ being the angle between the current direction and the wave vector direction.

For each wavenumber vector (k_x, k_y) in the wavenumber plane, a series of angular frequencies $(\omega_1, \omega_2, \ldots, \omega_{128})$ is associated. If the maximum energy within this set is lower than a predefined threshold, P, the corresponding set $(\omega_1, \omega_2, \ldots, \omega_{128})$ is discarded. For wavenumber vectors where the maximum energy exceeds the threshold, P, only one specific triplet (k_x, k_y, ω_i) corresponds to the ocean wave component that lies on the dispersion shell. This angular frequency, ω_i, is identified by detecting the most prominent energy peak in the series of frequencies for each wavevector. This procedure is applied to all wavenumber vectors (k_x, k_y), ultimately extracting the dispersion shell, $\omega(k_x, k_y)$.

3.3.3 Conversion to Polar Coordinates

Based on the fundamental relation, the frequency shift caused by the surface current is given by

$$\omega_U = \vec{k} \cdot \vec{U} = kU\cos(\theta_{ku}) \tag{3.2}$$

where ω_U is the Doppler-shifted angular frequency due to the current, k is the wavenumber magnitude, U is the magnitude of surface current speed, and θ_{ku} is the angle between the wave vector and the current direction.

Next, the Cartesian current shell $\omega_U(k_x, k_y)$ is transformed into polar coordinates to form the polar current shell, denoted as $\omega_U(k, \theta_k)$, where $k = \sqrt{k_x^2 + k_y^2}$ is the radial wavenumber, θ_k represents the direction of the wave vector in polar coordinates. This transformation allows for easier analysis of the surface current effects by examining the data along specific radii and angular directions.

3.3.4 Current Estimation Through Curve Fitting

To estimate the surface current, Grubbs' test [53] is applied to remove outliers along each radial direction. After eliminating the outliers, least-squares curve fitting is performed along the circumferential direction for each fixed radial wavenumber k. The fitting uses a sinusoidal model to determine the current speed, U, and direction, ϕ_U, minimizing the error cost function. The model function for curve fitting is given by

$$f(U, \overline{\theta_{ku}}) = \frac{\omega_U}{k} = U \cos \overline{\theta_{ku}} = U \cos(\theta_k - \phi_U). \tag{3.3}$$

The error cost function, which is minimized during the fitting process, is expressed as

$$E = \sum_{d=1}^{N_d} \left[\frac{\omega_{U_d}}{k} - U \cos(\theta_{k_d} - \phi_U) \right]^2 \tag{3.4}$$

where N_d is the number of points on the shell extracted in the circumferential direction for a specific k, θ_{k_d} is the wave vector direction, and ϕ_U is the surface current direction.

If the number of extracted shell points, N_d, for a specific wavenumber k is less than 10, the curve-fitting process for that k is terminated, and no results are retrieved for that wavenumber. The angle corresponding to the maximum value of the estimated function, $f(U, \overline{\theta_{ku}})$, is taken as the current direction, and the amplitude of the sinusoidal function represents the current speed. Finally, by averaging the results across different wavenumber magnitudes, a robust estimate of the current parameters is obtained.

3.3.5 Limitation Analysis

Based on our experiment, it was found that the original PCS method has some limitations. First, while Grubbs' test is used to detect outliers, not all instances of noise or aliasing appear as clear outliers. Second, curve fitting in the original method for a specific wavenumber k will be terminated if the number of data points available is less than 10, leading to a loss of potentially valuable data. This is not favorable, especially for sparse datasets. Since no fitting results are generated for these k-values, the accuracy of the method may be reduced. Moreover, if a specific k-value is strongly affected by noise, the fit result may be significantly biased. Then, during the final averaging step, these biased results can significantly affect the overall estimation, leading to a deviation from the true current parameters.

3.4 Improved PCS Method

Considering the potential issues with the original method, the improved PCS method incorporates several enhancements to increase the algorithm's accuracy and robustness. The original PCS method also has certain limitations, as discussed in Section 3.5. It is worth noting that the improved method performs an analysis for all wavenumber magnitudes within the polar current shell rather than conducting filtering and curve fitting for each wavenumber magnitude separately. The key improvements include better noise filtering, outlier rejection, and single curve fitting. These advancements address limitations in the original method, improving the precision of ocean current estimation.

3.4.1 Kernel Density Estimation-Based Direction Filtering

The KDE technique [54] is applied to estimate the density of the initial unfiltered data ($\mathbf{z}_i$) across all values of k in a specific direction, $i, i = 1, 2, 3, ..., 360$. As for the observed data points $\mathbf{z}_i$ in the ith direction, the estimated density, $\hat{f}_i(x)$, at a any point x within the domain of input data can be expressed as

$$\hat{f}_i(x) = \frac{1}{nh} \sum_{s=1}^{N_s} K\left(\frac{x - z_{i_s}}{h}\right) \tag{3.5}$$

where z_{i_s} is the sth data point in $\mathbf{z}_i$, $\mathbf{z}_i = [z_{i_1}, z_{i_2}, ..., z_{i_{N_s}}]$, N_s is the number of points in $\mathbf{z}_i$, h is the bandwidth parameter obtained by Silverman's rule [55], which can control the smoothness of the density estimate, and K is the Gaussian kernel function in this study. After calculating the density in each direction, data points, denoted as $\mathbf{z}_i^{'}$, within the range where the density in each direction exceeds half of the maximum density ($\hat{f}_i^{\max}(x) = \max(\hat{f}_i(x))$) are retained for further processing. Thus, the filtered data in all directions can be expressed as

$$\mathbf{Z}^{'} = [\mathbf{z}_1^{'}; \mathbf{z}_2^{'}; \mathbf{z}_3^{'}; ...; \mathbf{z}_{360}^{'}], \tag{3.6}$$

and the mean max density in all directions can be given by

$$\bar{f}^{\max}(x) = \frac{\sum_{i=1}^{360}(\hat{f}_i^{\max}(x))}{360}. \tag{3.7}$$

Then, those directions in $\hat{f}_i^{\max}(x)$ where the corresponding density value exceeds 60% of $\bar{f}^{\max}(x)$ are identified, and all data along these selected directions are extracted from $\mathbf{Z}^{'}$. The selected data can be denoted as $\mathbf{Z}_{f1}^{'}$ and utilized and analyzed for the subsequent steps.

This filtering step significantly reduces the influence of outliers and noise before the next filtering stage. By focusing on high-density regions, the algorithm ensures that the most reliable data are retained, improving the overall accuracy of current estimation.

3.4.2 Interquartile Range Noise Filtering

Once the high-density directions are identified from the filtered dataset, $\mathbf{Z}_{f1}^{'}$, obtained from the KDE process, IQR filtering [56] is applied as the next step to further refine the dataset. This filtering technique is used to remove outliers from the data in each direction, ensuring that the data better represent the underlying distribution.

For each direction, the interquartile range is calculated as

$$\mathrm{IQR} = Q_3 - Q_1 \tag{3.8}$$

where Q_1 is the 25th percentile (lower quartile) and Q_3 is the 75th percentile (upper quartile) of the data points $\mathbf{Z}_{f1}^{'}$. Data points are considered outliers if they fall below the lower bound or above the upper bound, defined as

$$\text{Lower bound} = Q_1 - 1.5 \times IQR \tag{3.9}$$

$$\text{Upper bound} = Q_3 + 1.5 \times IQR. \tag{3.10}$$

Any data points $\mathbf{Z}_i^{'}$ from $\mathbf{Z}_{f1}^{'}$ that fall outside the range $[\text{Lower bound}, \text{Upper bound}]$ are considered noise or outliers and are removed. The resulting filtered dataset, after applying IQR filtering, is denoted as $\mathbf{Z}_{f2}^{'}$.

This step ensures that outliers within the high-density regions are removed, further refining the dataset. Since the noise is significantly reduced, the filtered result $\mathbf{Z}_{f2}^{'}$ can improve the accuracy of subsequent curve fitting.

3.4.3 Symmetry-Based Opposite Direction Noise Reduction

After the IQR filtering in step 3.2, which identified and removed outliers from the dataset $\mathbf{Z}_{f1}^{'}$, symmetry-based opposite-direction noise reduction is applied. This step aims to reuse data points that may have been filtered out in the previous steps but are deemed reliable due to their symmetric counterparts in the data. At the same time, it also filters out data that do not satisfy the symmetry conditions, further refining the dataset.

The symmetry principle dictates that wavevectors that are symmetric around the origin should experience Doppler shifts of equal magnitude but with opposite signs [57]. For each pair of wavevectors $\vec{k}(k_x, k_y)$, its symmetric counterpart can be expressed as $\vec{k'}(-k_x, -k_y)$. According to Equation (3.2), the Doppler shift of the symmetric counterpart $\vec{k'}(-k_x, -k_y)$ becomes

$$\omega_u' = -kU\cos(\theta) \tag{3.11}$$

In an ideal, noise-free scenario, the sum of the Doppler shifts for symmetric wavevectors should be zero, i.e.,

$$\omega_u + \omega_u' = 0 \tag{3.12}$$

Figure 3.1 shows an example of the (a) intrinsic and (b) Doppler-shifted dispersion shells in the (k_x, k_y, ω) domain. A and B are two spectral points for two wavevectors symmetric about the origin of the wavenumber plane. In Figure 3.1a, their angular frequencies are shown to be the same, which are both ω_0. In Figure 3.1b, the Doppler shift of A is ω_{u_A}, and the Doppler shift of B is ω_{u_B}. In addition, the sum of ω_{u_A} and ω_{u_B} should be zero under ideal conditions. Also, Doppler shifts per unit wave number can be expressed by dividing both terms by k:

$$\frac{\omega_u}{k} + \frac{\omega'_u}{k} = 0 \tag{3.13}$$

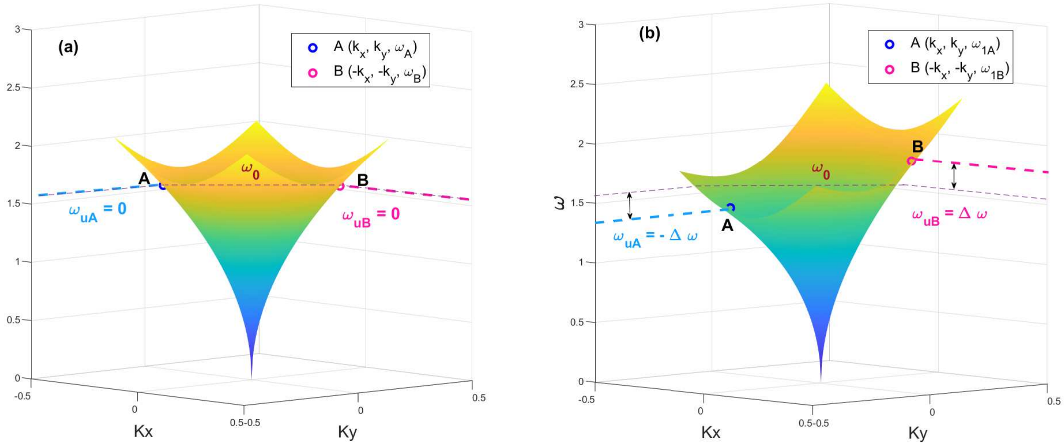

Figure 3.1: An example of the (**a**) intrinsic and (**b**) Doppler−shifted dispersion shells in the (k_x, k_y, ω) domain. Different colors represent the different ω values.

In this step, the algorithm calculates the difference in Doppler shifts per unit wavenumber between each pair of symmetric wavevectors:

$$S_\omega(\vec{k}, \vec{k'}) = \left| \frac{\omega_u}{k} + \frac{\omega'_u}{k} \right| \tag{3.14}$$

If the calculated difference, $S_\omega(\vec{k}, \vec{k'})$, is below a predefined threshold, the data point is retained. Specifically, the range of k values filtered out by IQR noise filtering is within the bounds of [Lower bound, Upper bound]. Therefore, for the wavevector $\vec{k'}$ symmetric to $\vec{k}$, the threshold for k' is set within the bounds of [−Upper bound, −Lower bound]. This ensures that the symmetry between $\vec{k}$ and $\vec{k'}$ is maintained, and that only data points satisfying this condition are retained for further analysis. This step ensures that any data points conforming to the symmetry principle are retained, while noise and inconsistencies are further filtered out. The final filtered dataset after applying this symmetry-based noise reduction is denoted as $\mathbf{Z}'_{f3}$. This refined dataset provides a more reliable basis for subsequent curve fitting.

3.4.4 Unified Curve Fitting for Filtered Data

After the data have been filtered, the improved PCS method applies a unified curve-fitting process to all the filtered data points, $k_1, k_2, \ldots, k_m$, which is the same as the curve-fitting process explained in Section 3.3.4. Unlike the original PCS method, where curve fitting was performed separately for different radii k, the improved method fits a single sinusoidal curve to the entire filtered dataset, $\mathbf{Z}'_{f3}$. This approach minimizes the potential for localized fitting errors and ensures that the final current speed and direction estimates are more consistent and accurate across the entire wave spectrum. Unified fitting also helps to reduce the impact of aliasing by incorporating a broader range of reliable data into the curve-fitting process.

3.5 Experiments and Results

3.5.1 Experiment on Simulated Data

This section contains a description of experiments which were conducted using radar data simulated under two different antenna rotation speeds (RPM: 24 and 48). The simulated radar data is generated using a modified PM wave spectrum [38] integrated with a cardioid directional spreading function [39, 58]. To simulate ocean current effects, additional parameters were introduced into the dataset to include surface currents with specific speeds and directions. The simulated dataset includes two files: one corresponding to an antenna rotation speed of 24 RPM, and a current speed range between 0.5 and 10 m/s with a current direction of 150°, and another file with a 48 RPM rotation speed, covering a current speed range from 0.5 to 15 m/s and a current direction of 180°. These high encounter velocities are used to test the method's robustness in extreme scenarios, such as fast-moving ships or strong currents, which may not be typical for average ocean surface currents but are crucial for validating the algorithm's performance under challenging conditions. These files were processed using three different methods, PCS, improved PCS, and NSP, to evaluate each method's performance under different sea state conditions.

Limitation Analysis and Improvement

To analyze the limitations of the original PCS method and demonstrate the improvements introduced by the improved PCS method, one radar image file from the 24 RPM simulated data series, as shown in Figures 3.2 and 3.3, is selected as an example. The encounter velocity in this simulation is 7.5 m/s, and the current direction is 150°. In the simulation, noise is incorporated through the addition of random phase components in the frequency domain. This approach introduces a uniformly distributed random phase between 0 and 2π for each component. By applying these random phases to the complex spectrum before the inverse Fourier transform, the inherent randomness are simulated in real radar echoes. This method effectively mimics the various noise sources encountered in actual radar systems, including environmental factors, system imperfections, and signal fluctuations. Regarding aliasing, the simulated speeds were intentionally selected to represent a broad range of possible conditions, including extreme cases. Aliasing will occur if the speeds were high with a low sampling rates. In most cases, aliasing cannot be avoided.

(a) Analysis of original PCS results Figure 3.2a shows all the data after being converted to the PCS domain, plotted against different k values. This represents the raw data before any outlier removal or filtering is applied. The spread of data points indicates significant noise and aliasing, especially at higher k values. Figure 3.2b presents the data after applying the original PCS method's outlier removal process. Here, some of the noise has been removed by the original PCS method, but outliers are still present, particularly in regions with higher variability, suggesting that the original outlier removal process is not fully effective. Figure 3.2c shows the curve-fitting results for different k vectors after applying the original PCS method. The curve fitting is highly impacted by the remaining outliers and noise, leading to significant deviations in current speed and direction estimations. Although averaging all the fitted results can improve the results a little bit, the overall poor fit highlights the limitations of the original PCS method in handling low-RPM scenarios and noisy data.

(b) Analysis of improved PCS results Figure 3.3a shows all the data after being converted to the PCS domain, similar to Figure 3.2a. This serves as the starting point before applying any filtering or noise reduction techniques in the improved PCS method. The data still exhibit significant noise and variability, particularly at higher k values. Figure 3.3b presents the data after applying KDE-based direction filtering. KDE helps to highlight the most probable directions by reducing the influence of extreme outliers, resulting in a more concentrated and reliable data distribution compared to the unfiltered data in Figure 3.3a. Figure 3.3c shows the data after applying IQR noise filtering. The IQR filtering process further refines the data by removing points that fall outside the interquartile range, which are likely to be noise or outliers. The data appear more consistent and aligned, indicating a significant reduction in noise. Figure 3.3d shows the data after restoring certain points filtered out by the IQR method. Specifically, points that had been removed due to their low density but satisfy the symmetry with high-density directional values are recovered. This results in a dataset that is both clean and retains important symmetric information, making it more comprehensive than the one shown in Figure 3.3c.

Finally, Figure 3.3e presents the unified curve fitting for the filtered data. After applying all the filtering techniques, the final curve-fitting process is applied, resulting in a smooth, well-fitted curve that accurately represents the current speed and direction. The improved PCS method's curve fitting is much more precise compared to the original method, as shown by the reduced deviation and noise.

The improved PCS method significantly reduces the influence of outliers and noise, as evidenced by the tighter clustering of data points and the smoother curve fitting observed in the final result. The aliasing effects seen in the original method have also been largely mitigated, providing a more accurate representation of the current speed and direction.

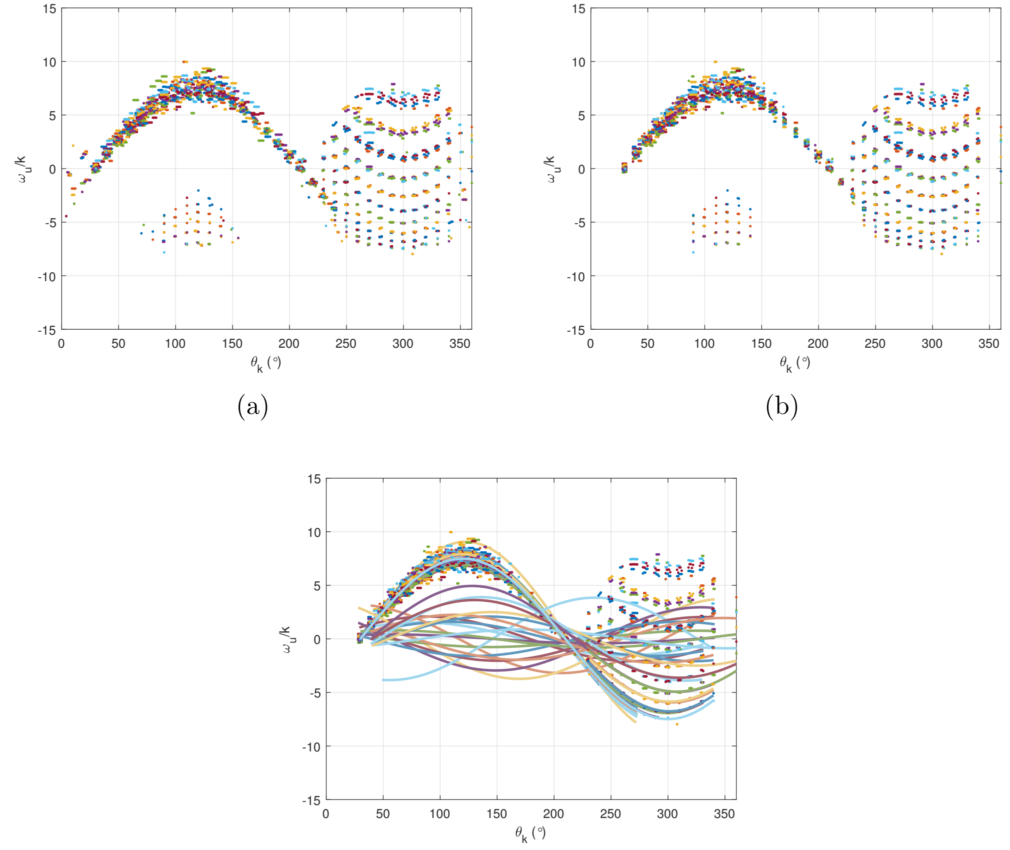

(a)

(b)

(c)

Figure 3.2: (**a**) Description of all the data after converting to the polar current shell (PCS) domain. (**b**) Description of the data after applying the original PCS method's outlier removal process. (**c**) Description of the curve−fitting results for different k vectors. Different colors correspond to different values of wavenumber k.

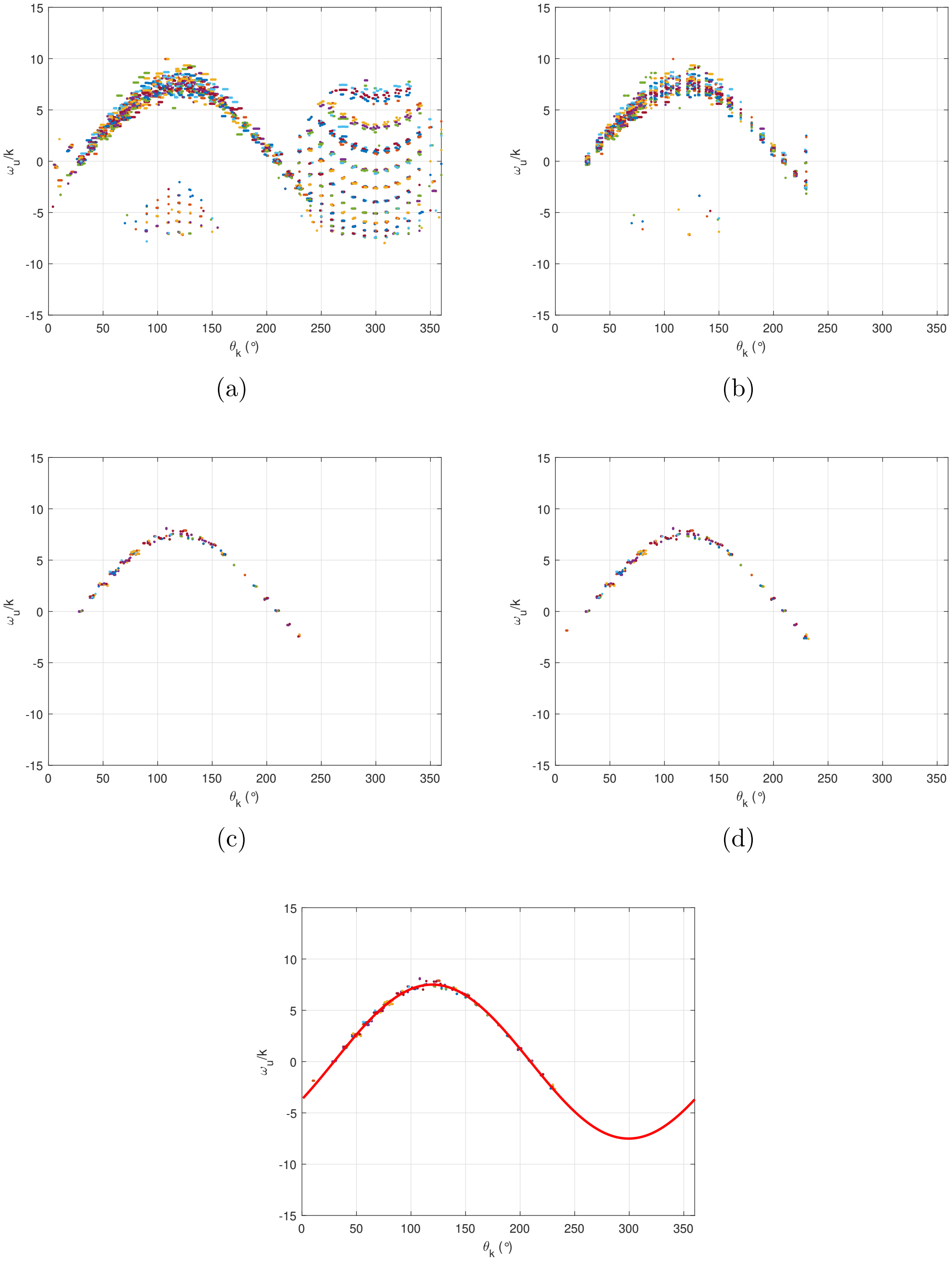

(a)

(b)

(c)

(d)

(e)

Figure 3.3: Description of (**a**) all the data after converting to the PCS domain, (**b**) KDE−based direction−filtering result, (**c**) interquartile range noise filtering result, (**d**) symmetry−based opposite direction noise reduction result, and (**e**) unified curve fitting for filtered data.

Analysis of the Results

The results are shown in Figure 3.4 and Table 3.1, which illustrate the performance of the original and improved PCS methods under two different RPM conditions (24 and 48 RPM).

In Figure 3.4, different methods are represented by distinct markers: a blue * indicates the results of the NSP method, a black x represents the results of the original PCS method, and red circles stand for the results of the improved PCS method. The solid line represents the true values. The graphs depict the retrieved current speed and direction against the input speed for two different rotation speeds, 24 RPM and 48 RPM. Table 3.1 presents the error analysis of the simulated data, including the CCs and RMSD for speed and direction estimates. It shows the performance of each method in terms of speed and direction accuracy across different RPM values. A noticeable observation from Figure 3.4 and Table 3.1 is that the original PCS method exhibits significant errors at 24 RPM, particularly in current speed estimation. The improved PCS method, in contrast, consistently delivers better accuracy, as reflected in the smaller RMSD values and higher correlation with the true values.

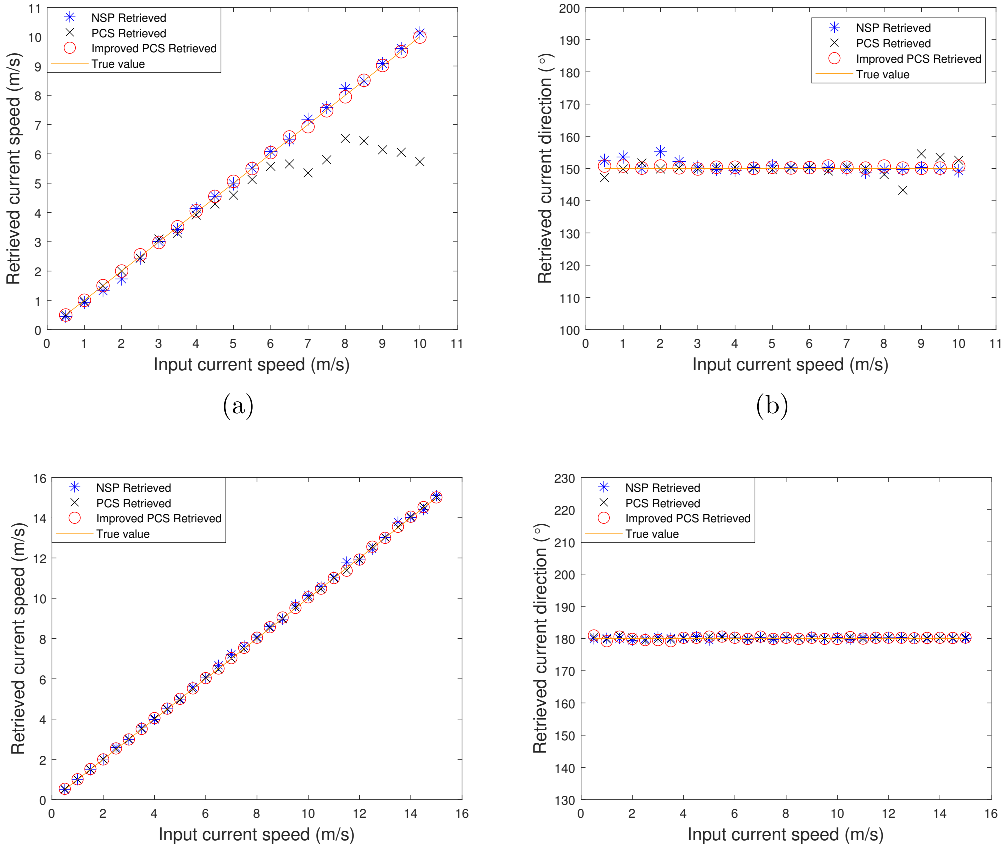

(a)
(b)
(c)
(d)

Figure 3.4: (**a**) Retrieved current speed versus input speed at revolutions per minute (RPM) = 24. (**b**) Retrieved current direction versus input speed at RPM = 24. (**c**) Retrieved current speed versus input speed at RPM = 48. (**d**) Retrieved current direction versus input speed at RPM = 48.

Table 3.1: Error analysis of simulated data.

File	RPM	Method	CC		RMSD		Current Speed Range [m/s]	Current Direction [°]
			Speed	Direction	Speed [m/s]	Direction [°]		
1	24	PCS	0.93	1	0.86	2.8	0.5–10	150
		Improved PCS	1	1	0.07	0.8		
		NSP	0.96	1	0.09	0.9		
2	48	PCS	1	1	0.06	0.7	0.5–15	180
		Improved PCS	1	1	0.04	0.4		
		NSP	1	1	0.08	1.1		

(a) Estimated result comparison at 24 RPM At 24 RPM, as shown in Figure 3.4a,b, the original PCS method suffers from noticeable deviations in both speed and direction estimates. Specifically, the speed estimate tends to diverge significantly as the input speed increases beyond 5 m/s, as illustrated by the blue x in Figure 3.4a. The improved PCS method, represented by red circles, significantly reduces these deviations, providing results much closer to the true values (the solid line). This is further confirmed in Table 3.1, where the speed RMSD of the improved PCS method is 0.07 m/s, compared to 0.86 m/s for the original PCS.

For current direction, as shown in Figure 3.4b, the original PCS method maintains relatively consistent direction estimates at lower speeds but shows more pronounced deviations at higher input speeds. The improved PCS method also performs better than the original, with an RMSD of 0.8° compared to 2.8° for the original PCS. The green x representing the NSP method provides more accurate estimates than the original PCS but remains less accurate than the improved PCS method.

The increased error in the original PCS method at 24 RPM can be attributed to the lower temporal resolution associated with the slower antenna rotation speed. At 24 RPM, fewer radar sweeps are performed per second, reducing the temporal frequency of data collection.

Physically, this limitation affects high-speed currents where rapid changes in current speed and direction are harder to capture with fewer data points. As the input current speed increases beyond 5 m/s, the original PCS method struggles to accurately track these rapid variations, leading to significant deviations in both speed and direction estimates.

In contrast, the improved PCS method incorporates advanced noise filtering techniques, such as Kernel Density Estimation (KDE) and interquartile range (IQR) filtering. These techniques effectively reduce noise and improve data reliability, especially at lower sampling frequencies. KDE enhances the detection of dominant directional densities, mitigating the impact of random noise, while IQR filtering removes outliers that could otherwise distort curve fitting. Additionally, the unified curve-fitting process introduced in the improved PCS method ensures consistent parameter estimation across the entire radar spectrum, reducing the susceptibility to errors caused by uneven data distribution.

(b) Estimated result comparison at 48 RPM At 48 RPM, the performance of the original PCS method improves significantly, as depicted in Figure 3.4c,d. The speed and direction estimates become more reliable compared to the results at 24 RPM, with an RMSD of 0.06 m/s for speed and 0.7° for direction. However, the improved PCS method still shows less error, with an RMSD of 0.04 m/s for speed and 0.4° for direction, as shown in Table 3.1. The green x representing the NSP method also provides reasonable accuracy but remains less effective than the improved PCS method.

The improvement observed in the original PCS method at 48 RPM can be attributed to the higher temporal resolution provided by the faster antenna rotation speed. Physically, this allows the radar to capture more frequent data points, enhancing its ability to track rapid variations in ocean currents. Despite this improvement, the original PCS method's segmented curve-fitting process still introduces inconsistencies across different wavenumber magnitudes, limiting its overall accuracy. The improved PCS method outperforms both the original PCS and NSP methods due to its unified curve-fitting process and robust noise filtering techniques. The unified approach reduces computational overhead while maintaining consistent accuracy across all data points. Furthermore, its symmetry-based noise reduction method leverages the physical property of wave symmetry in the Doppler shift, ensuring more reliable data extraction under dynamic conditions.

3.5.2 Experiment on Real Data

This section provides an overview of the real-world validation performed using radar data from various sea trials.

Analysis of Decca Radar Data

(a) Data description The first dataset analyzed in this study was provided by Defence Research and Development Canada (DRDC) and collected during a sea trial from 25 November to 4 December 2008, approximately 220 km off the coast of Halifax. The experiment utilized HH-polarized shipborne Decca marine radars, operating at a frequency of 9.41 GHz and covering a full 360° azimuth. For the purpose of this study, the radar data had a maximum range of 2160 m and a range resolution of 7.5 m. Excluding the completely black images with no wave signature caused by system errors, a total of 2041 radar images were analyzed. The radar signals were processed using the WaMoS II, which digitized them into 8-bit image intensities. The surface current data obtained from the WaMoS II system serve as a reference for validating the accuracy of our algorithm in estimating ocean surface currents.

(b) Comparison of encounter current velocity estimation Since the radar data were collected from a moving ship in this study, the encounter current is analyzed first. Encounter current refers to the relative current experienced by the moving ship, as it moves through the sea. This is the combined effect of the actual surface current and the movement of the ship itself. The comparison of the encounter current estimation results between the improved PCS, PCS, and NSP methods is shown in Figure 3.5. The range of $-40°$ to $400°$

in Figure 3.5b is set to avoid oscillations or abrupt changes in the estimated direction near the 0° and 360° boundaries. Directional data often wrap around at 0° or 360°, which can cause sudden jumps or oscillations when visualized. By extending the range beyond the typical 0–360° range, this issue is mitigated, allowing for a smoother representation of the directional estimates.

As recorded in Table 3.2, the CC between the speed estimates from the improved PCS method and the reference WaMos data is 0.99, which is higher than that (0.92) of the original PCS method and that (0.91) of the NSP method. The improved PCS algorithm has an RMSD of 0.38 m/s, whereas the original PCS and NSP methods show higher RMSD values of 0.51 m/s and 1.14 m/s, respectively. The improved PCS estimates are closely aligned with the reference WaMos data, while the original PCS and NSP methods shows higher deviations, particularly in areas with significant speed changes. Higher CC and lower RMSD values were obtained for the improved PCS method.

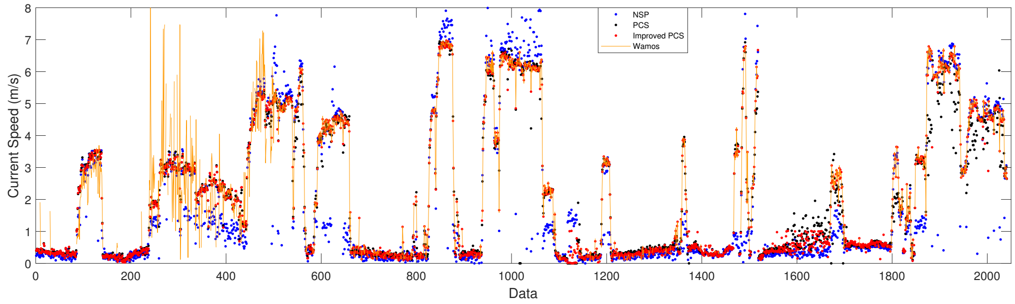

(a)

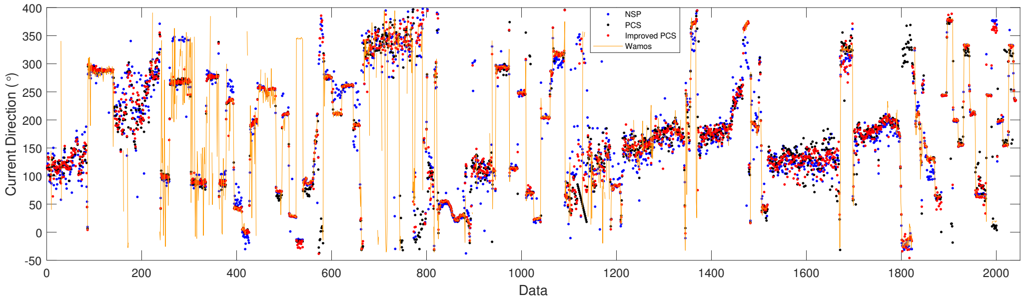

(b)

Figure 3.5: (**a**) Comparison of encounter current speed and (**b**) encounter current direction obtained from Decca radar data.

Table 3.2: Error analysis of encounter current estimation based on 2008 radar data.

Method	**CC**		**RMSD**	
	Speed	**Direction**	**Speed [m/s]**	**Direction [°]**
Improved PCS	0.99	0.93	0.38	20.3
PCS	0.92	0.90	0.51	24.6
NSP	0.91	0.91	1.14	25.2

The improved PCS method has a CC of 0.93 for current direction and is superior to the PCS (0.90) and NSP (0.91) methods. For RMSD, the improved PCS algorithm has the lowest error of 20.3°, compared to 24.6° for PCS and 25.2° for NSP. Figure 3.5b demonstrates that the original PCS method shows some deviation in sections with directional shifts. In contrast, the improved PCS method aligns with the WaMos reference.

(c) Motion compensation To accurately estimate the surface current from the radar data, it is essential to account for the ship's motion by subtracting the ship's speed from the encounter current (U_{en}). However, as noted by Bell and Osler [25], inconsistencies in the ship's speed within certain radar image sequences can create difficulties in determining the true ship speed. Figure 3.6 shows an example of these inconsistencies in ship speed data recorded during the radar data collection process.

Bell and Osler [25] proposed a method for georeferencing radar data by correcting ship heading errors using high-resolution GPS and heading data, synchronized with the ship's network. Lund et al. [24, 26] expanded this approach by applying georeferencing to each radar pulse individually, accounting for ship motion and heading variations. Gangeskar [27] demonstrated the effectiveness of real-time motion compensation using vessel motion data (e.g., GPS, gyroscope) to ensure accurate radar-derived surface current estimates, even in moving installations. Together, these methods greatly enhance radar accuracy in dynamic environments.

Building on these methods, the starting position, ship speed, and heading for each radar image sequence are used in our approach. Each radar pixel is mapped to a geographic reference frame, from which sub-image sequences are extracted to enhance the accuracy of motion compensation during surface current estimation.

Figure 3.7 shows the effect of motion compensation. In Figure 3.7a, the sub-region is extracted from the radar image before motion compensation, where distortions are visible due to vessel movement. In contrast, Figure 3.7b presents the same sub-region after applying motion compensation, showing a clearer and more stable region. The compensation process corrects the distortions caused by the ship's movement, providing more accurate data for further analysis.

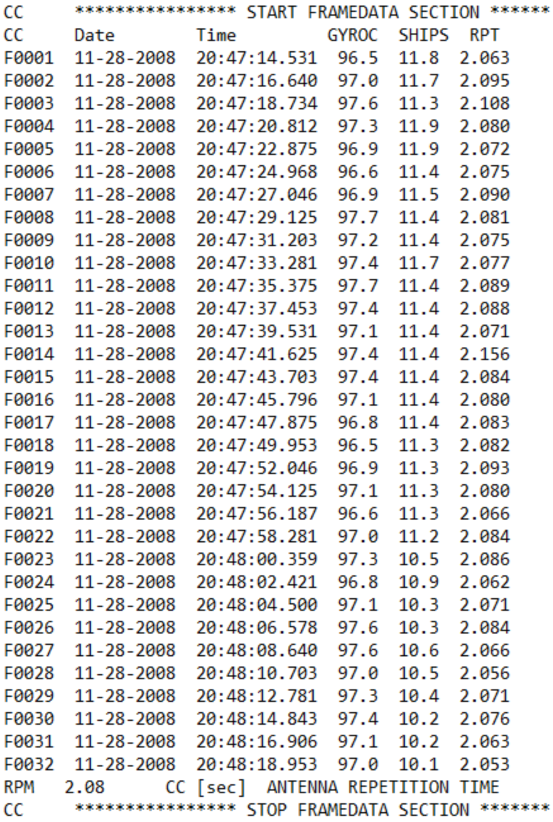

```
CC     **************** START FRAMEDATA SECTION ******
CC     Date        Time         GYROC  SHIPS  RPT
F0001  11-28-2008  20:47:14.531  96.5  11.8  2.063
F0002  11-28-2008  20:47:16.640  97.0  11.7  2.095
F0003  11-28-2008  20:47:18.734  97.6  11.3  2.108
F0004  11-28-2008  20:47:20.812  97.3  11.9  2.080
F0005  11-28-2008  20:47:22.875  96.9  11.9  2.072
F0006  11-28-2008  20:47:24.968  96.6  11.4  2.075
F0007  11-28-2008  20:47:27.046  96.9  11.5  2.090
F0008  11-28-2008  20:47:29.125  97.7  11.4  2.081
F0009  11-28-2008  20:47:31.203  97.2  11.4  2.075
F0010  11-28-2008  20:47:33.281  97.4  11.7  2.077
F0011  11-28-2008  20:47:35.375  97.7  11.4  2.089
F0012  11-28-2008  20:47:37.453  97.4  11.4  2.088
F0013  11-28-2008  20:47:39.531  97.1  11.4  2.071
F0014  11-28-2008  20:47:41.625  97.4  11.4  2.156
F0015  11-28-2008  20:47:43.703  97.4  11.4  2.084
F0016  11-28-2008  20:47:45.796  97.1  11.4  2.080
F0017  11-28-2008  20:47:47.875  96.8  11.4  2.083
F0018  11-28-2008  20:47:49.953  96.5  11.3  2.082
F0019  11-28-2008  20:47:52.046  96.9  11.3  2.093
F0020  11-28-2008  20:47:54.125  97.1  11.3  2.080
F0021  11-28-2008  20:47:56.187  96.6  11.3  2.066
F0022  11-28-2008  20:47:58.281  97.0  11.2  2.084
F0023  11-28-2008  20:48:00.359  97.3  10.5  2.086
F0024  11-28-2008  20:48:02.421  96.8  10.9  2.062
F0025  11-28-2008  20:48:04.500  97.1  10.3  2.071
F0026  11-28-2008  20:48:06.578  97.6  10.3  2.084
F0027  11-28-2008  20:48:08.640  97.6  10.6  2.066
F0028  11-28-2008  20:48:10.703  97.0  10.5  2.056
F0029  11-28-2008  20:48:12.781  97.3  10.4  2.071
F0030  11-28-2008  20:48:14.843  97.4  10.2  2.076
F0031  11-28-2008  20:48:16.906  97.1  10.2  2.063
F0032  11-28-2008  20:48:18.953  97.0  10.1  2.053
RPM   2.08      CC [sec]  ANTENNA REPETITION TIME
CC     **************** STOP FRAMEDATA SECTION *******
```

Figure 3.6: Ship speed recorded during the radar data collection process.

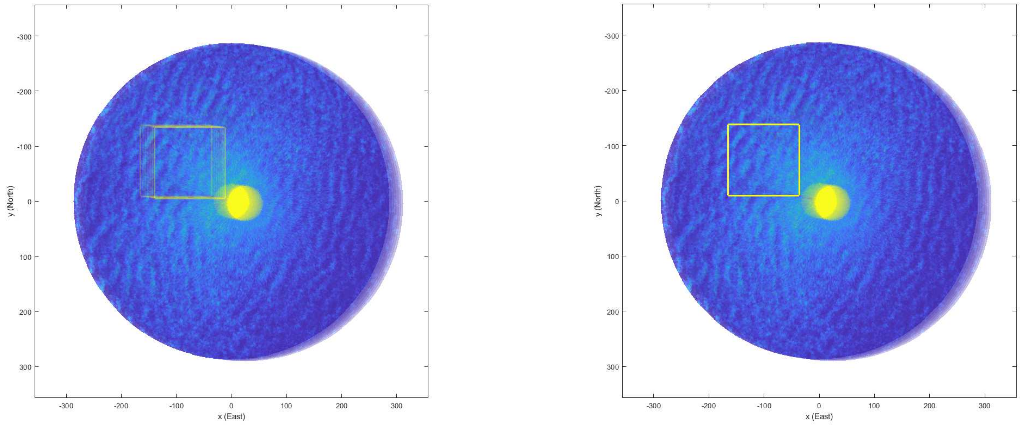

(a)

(b)

Figure 3.7: (**a**) The extracted sub−region (framed in yellow square) before motion compensation. (**b**) The extracted sub−region (framed in yellow square) after motion compensation.

(d) Surface current estimation analysis After applying motion compensation to eliminate the effects of ship movement, the surface current was directly extracted from the motion-compensated radar imagery. Figure 3.8a shows the comparison of surface current speed, and Figure 3.8b displays the comparison of surface current direction. The results are based on sub-regions of the radar image that have been motion-compensated, ensuring that errors caused by ship movement have been minimized. In Figure 3.8a, the improved PCS method closely follows the true values, with fewer fluctuations and deviations, especially in regions where the surface current speed changes rapidly, while the original PCS method and NSP method exhibit larger discrepancies. Similarly, in Figure 3.8b, the improved PCS method delivers a more precise estimation of surface current direction, particularly in regions with sharp directional changes. The original PCS and NSP methods, even after motion compensation, struggle to maintain the same level of accuracy in these areas. This enhanced accuracy can be attributed to its advanced spectral analysis techniques, robust noise suppression, and improved handling of non-linear wave-current interactions, which are especially effective when processing real-world X-band radar data.

Figure 3.9a,c,e show the distribution of the differences in the east (x) and north (y) components of the current vector obtained by WaMos and the improved PCS, PCS, and NSP methods. The colour intensity of each scatter point represents the corresponding WaMos-measured surface current speed. Moreover, Figure 3.9b,d,f present the relationship between the WaMos current directions (indicated by different colour intensities) and the error distribution for different methods. The improved PCS method exhibits minimal error dispersion. This tight clustering highlights the method's reliability across different speed conditions, with errors remaining small even at high speeds. The PCS method shows a relatively wider error spread, indicating that it may be more sensitive to variations in current speed compared to the improved PCS method. In contrast, the NSP method has the broadest error range for the data used in this study. The spread increases, particularly for high-speed conditions.

Table 3.3 provides the error analysis of surface current estimation based on the 2008 radar data. The improved PCS method, which includes motion compensation, achieves the highest CC in both speed (0.85) and direction (0.88), along with the lowest RMSD values for speed (0.08 m/s) and direction (26.9°). In comparison, the original PCS method exhibits slightly lower CCs and higher RMSD values.

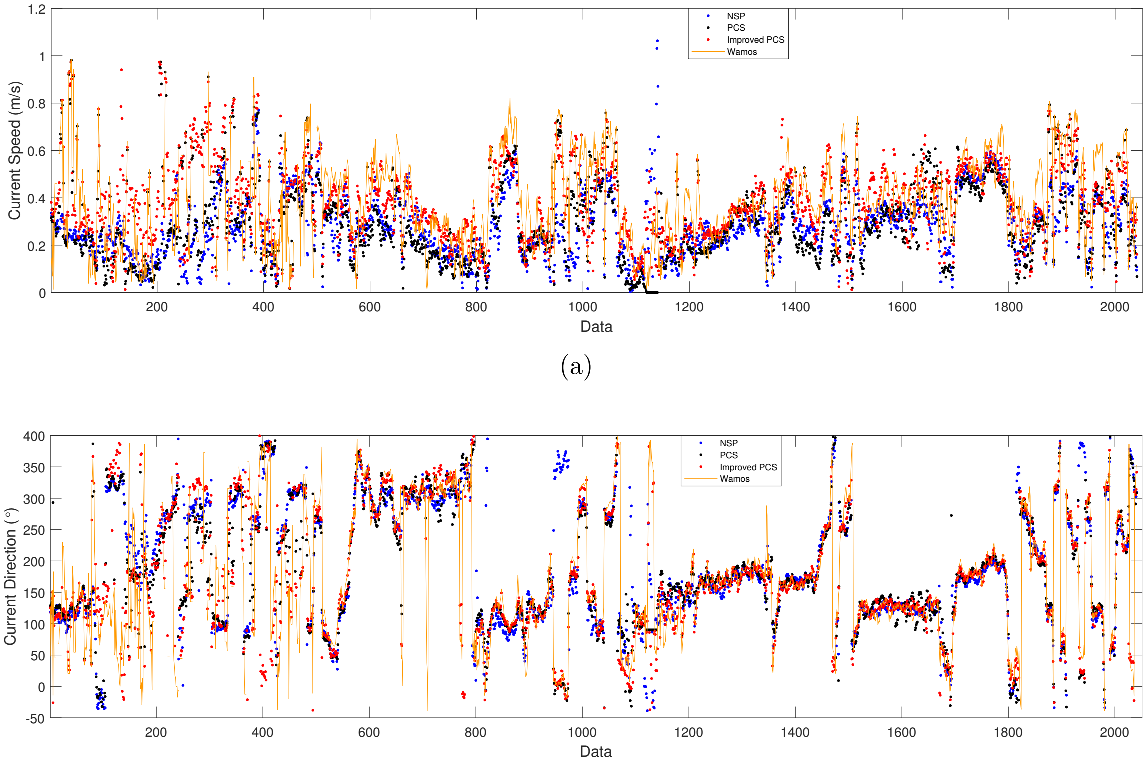

(a)

(b)

Figure 3.8: (**a**) Comparison of surface current speed and (**b**) surface current direction obtained from Decca radar data.

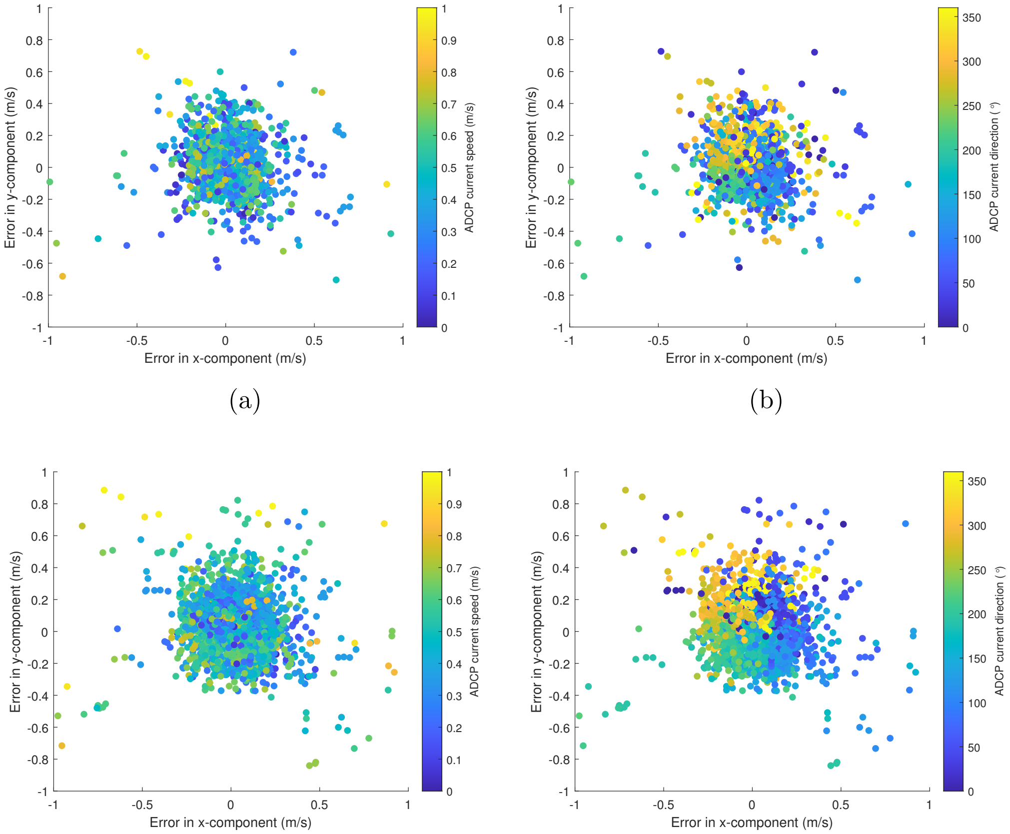

(a) (b)

(c) (d)

Figure 3.9: *Cont.*

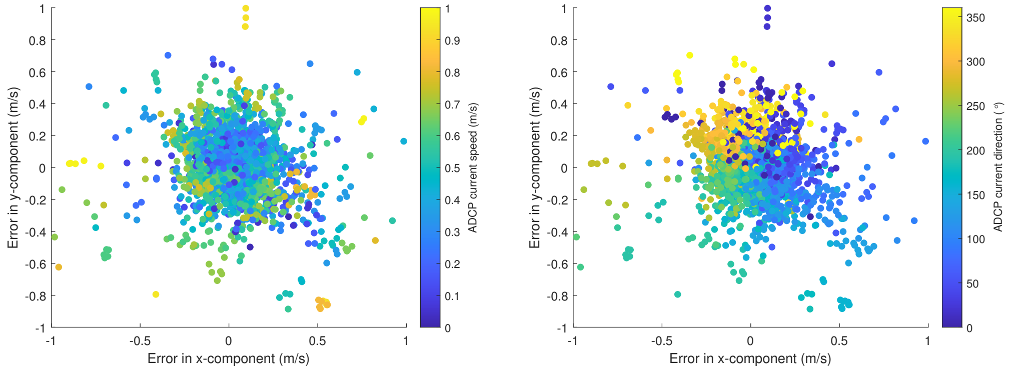

(e) (f)

Figure 3.9: Scatter plot of the difference in the east (x) and north (y) components of the current vector measured by WaMos and the radar along with the corresponding surface current speed using the (**a**) improved PCS, (**c**) PCS, and (**e**) NSP methods, along with the corresponding surface current direction using the (**b**) improved PCS, (**d**) PCS, and (**f**) NSP methods.

Table 3.3: Error analysis of surface current estimation based on Decca radar data.

Method	**CC**		**RMSD**	
	Speed	**Direction**	**Speed** [m/s]	**Direction** [°]
Improved PCS	0.85	0.88	0.08	26.9
PCS	0.79	0.81	0.14	30.7
NSP	0.74	0.76	0.18	34.3

Analysis of Koden Radar Data

(a) Data description The radar data for this study were acquired from an X-band Koden marine radar system mounted on a 106-foot mobile tower at Guadalupe Dunes, CA, USA [59]. The data were collected between 15 September and 23 October 2017. The radar system operates at a frequency of 9.45 GHz, utilizing horizontal transmit and horizontal receive polarization (HH) for both the transmission and reception of radar pulses. Only radar images captured during periods with wind speeds exceeding 3 m/s and moderate-to-high sea states were included in the analysis. This filtering process was implemented because radar backscattering at wind speeds below 3 m/s is significantly weaker, making it difficult to observe clear wave signatures on the radar images. The resulting dataset comprised 2713 valid radar images, which were used for surface current estimation. The reference data are the 30 s block-averaged quality-controlled ADCP data [60].

(b) Surface current comparison In the analysis of the 2017 radar data, shown in Table 3.4 and Figure 3.10, the improved PCS method demonstrates superior performance in estimating surface current speed and direction compared to both the PCS and NSP methods. It should be noted that after applying a 3D FFT and subsequent energy filtering, the amount of data that remained after being converted to the PCS domain was significantly reduced. This reduction is primarily due to the relatively small variation in wave direction energy caused by the surface current motion in this dataset. One possible reason for this small variation could be the specific sea-state conditions during the data collection period, where lower wind speeds or calmer seas resulted in less pronounced wave-current interactions. As a result, the surface current-induced changes in wave direction energy were not as pronounced as in other datasets, leading to fewer effective data points in the PCS domain. Due to this limitation, the overall accuracy of the surface current estimations from this dataset was lower compared to the Decca radar data. Data points with poor quality, where the PCS algorithm fails to estimate results, are excluded from the error analysis. As illustrated in Figure 3.10a, the retrieved current speed using the improved PCS method closely aligns with the ADCP data, particularly in regions where the current undergoes significant dynamic changes. The RMSD for the improved PCS method is 0.09 m/s, which is slightly lower than for the PCS (0.11 m/s) and NSP (0.12 m/s) methods, as shown in Table 3.4. Similarly, the surface current direction estimates shown in Figure 3.10b reflect the improved PCS method's better performance. The RMSD for current direction is reduced to 30.1° for the improved PCS method, compared to 34.7° for PCS and 35.1° for NSP. The scatter plots shown in Figure 3.11 provide a visual comparison of the retrieved current speed and direction against the reference ADCP data for three different methods: improved PCS, PCS, and NSP. In Figure 3.11a,b, the improved PCS method demonstrates a high degree of correlation between the retrieved current speed and direction and the ADCP reference values, as evidenced by the close clustering of data points along the 1:1 line. This suggests that the improved algorithm yields more accurate results in both speed and direction estimations.

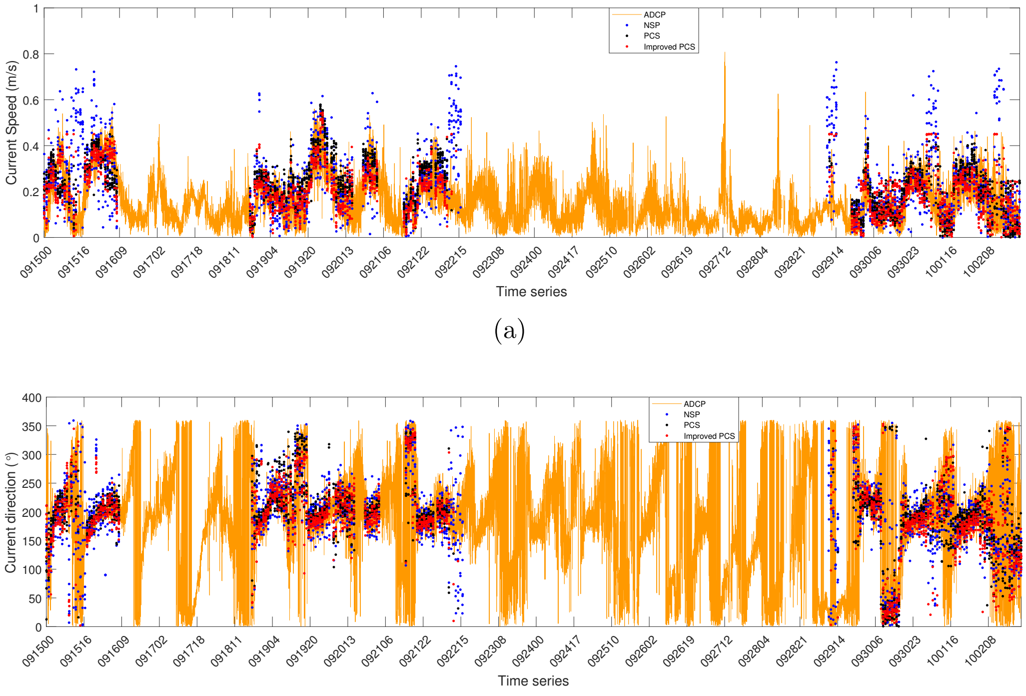

Figure 3.10: (**a**) Comparison of surface current speed and (**b**) surface current direction obtained from Koden radar data.

Table 3.4: Error analysis of surface current estimation based on Koden radar data.

Method	**CC**		**RMSD**		**Bias**	
	Speed	**Direction**	**Speed [m/s]**	**Direction [°]**	**Speed [m/s]**	**Direction [°]**
Improved PCS	0.75	0.82	0.09	30.1	0.01	−2.8
PCS	0.72	0.77	0.11	34.7	0.04	−3.9
NSP	0.70	0.73	0.12	35.1	0.06	−4.3

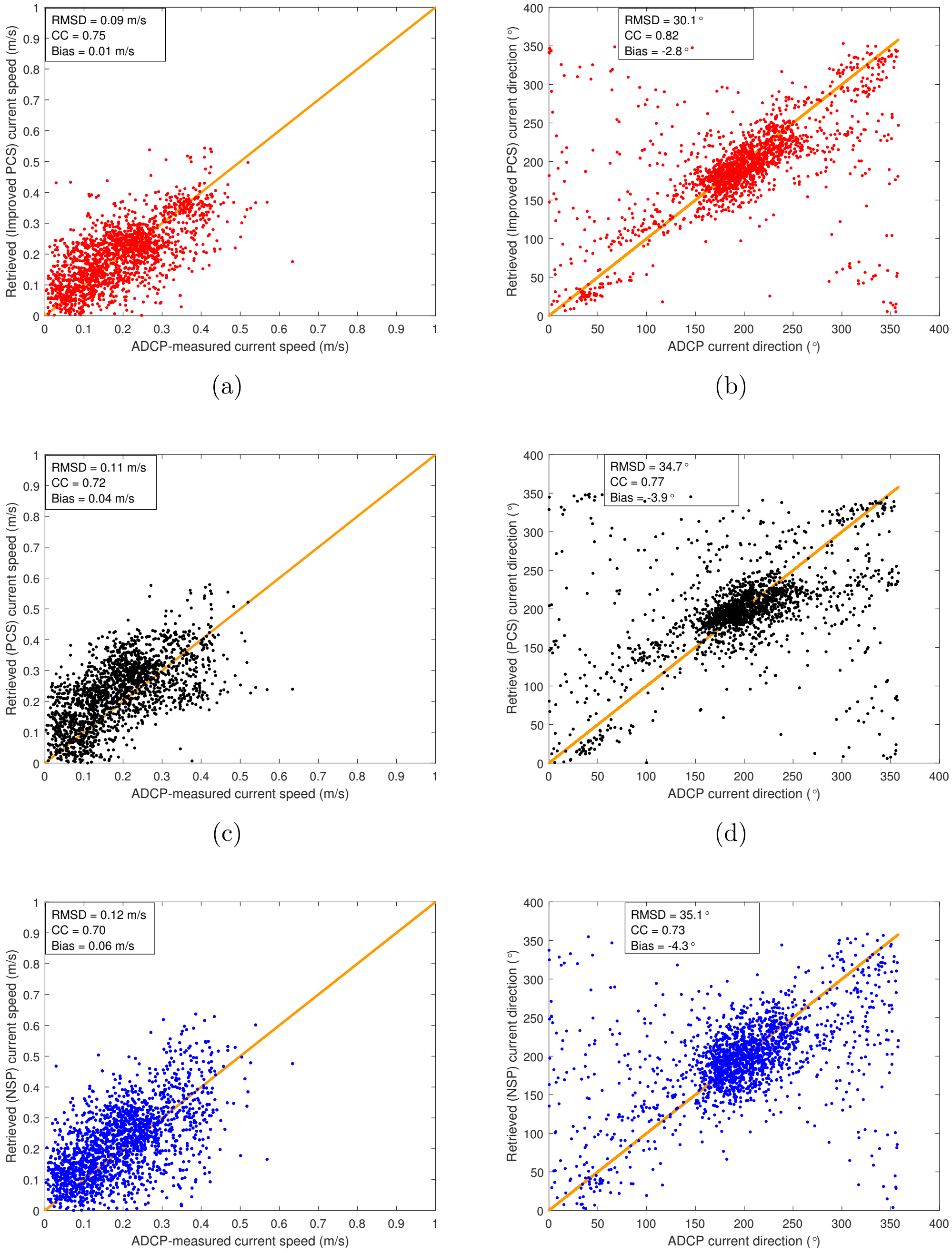

(a) (b)

(c) (d)

(e) (f)

Figure 3.11: (**a**) Scatter plot comparing ADCP current speed to the retrieved current speed using the improved PCS method. (**b**) Scatter plot comparing ADCP current direction to the retrieved current direction using the improved PCS method. (**c**) Scatter plot comparing ADCP current speed to the retrieved current speed using the PCS method. (**d**) Scatter plot comparing ADCP current direction to the retrieved current direction using the PCS method. (**e**) Scatter plot comparing ADCP current speed to the retrieved current speed using the NSP method. (**f**) Scatter plot comparing ADCP current direction to the retrieved current direction using the NSP method.

For the PCS method, shown in Figure 3.11c,d, a larger spread of points is observed, particularly in the current direction plot (d), indicating greater discrepancies between the retrieved values and the ADCP reference values. This lower accuracy compared to the improved PCS method can be attributed to several factors, including higher susceptibility to noise and interference, limited capability in handling complex wave-current interactions, and less sophisticated spectral analysis techniques. Additionally, the traditional PCS method may struggle with distinguishing between wave-induced and current-induced Doppler shifts, especially in challenging sea state conditions.

In the NSP method's results, illustrated in Figure 3.11e,f, an even wider spread is noticeable, especially in the plot (f) for the current direction, where data points are significantly scattered, further highlighting the poorer performance of this method in accurately estimating the current direction when compared to both PCS and improved PCS.

In addition, the scatter plot of the differences in the east (x) and north (y) components of the current vector obtained by ADCP and the radar are presented in Figure 3.12, along with the ADCP-derived surface current speed and direction. The improved PCS method shows errors that are closest to zero in both the x and y components. The original PCS method has a broader error range, especially along the x-axis. In contrast, the NSP method has the largest error scope. Overall, it can be observed that the improved PCS is the most accurate. This analysis underscores the higher accuracy of the improved PCS method in estimating both current speed and direction, as reflected by the tighter clustering of points around the ADCP reference line. Even for a dataset with lower overall precision, the improved PCS method consistently maintains the highest level of accuracy compared to other methods.

The improved PCS method's superior performance can be attributed to its advanced data processing techniques and robust modelling capabilities. The improved PCS method employs a unified curve-fitting process for all filtered data points, unlike the original PCS method which performs curve fitting separately for different radii. This unified approach ensures that the entire current speed and direction estimates are consistent and accurate across the entire wave spectrum. By fitting a single sinusoidal curve to the entire filtered dataset, the improved PCS method effectively minimizes the potential fitting errors associated with curve fitting for each k value, and reduces the impact of aliasing, thereby incorporating a broader range of reliable data into the curve-fitting process. Furthermore, the method's ability to handle high encounter velocities, as tested in extreme scenarios with fast-moving ships or strong currents, demonstrates its robustness under challenging conditions. These advanced techniques enable the improved PCS method to effectively distinguish between wave-induced and current-induced Doppler shifts, even in complex sea states, leading to more precise and reliable ocean surface current estimations. Overall, the combination of effective noise reduction, comprehensive modeling, and sophisticated spectral analysis underpins the improved PCS method's higher accuracy and reliability compared to traditional PCS and NSP methods.

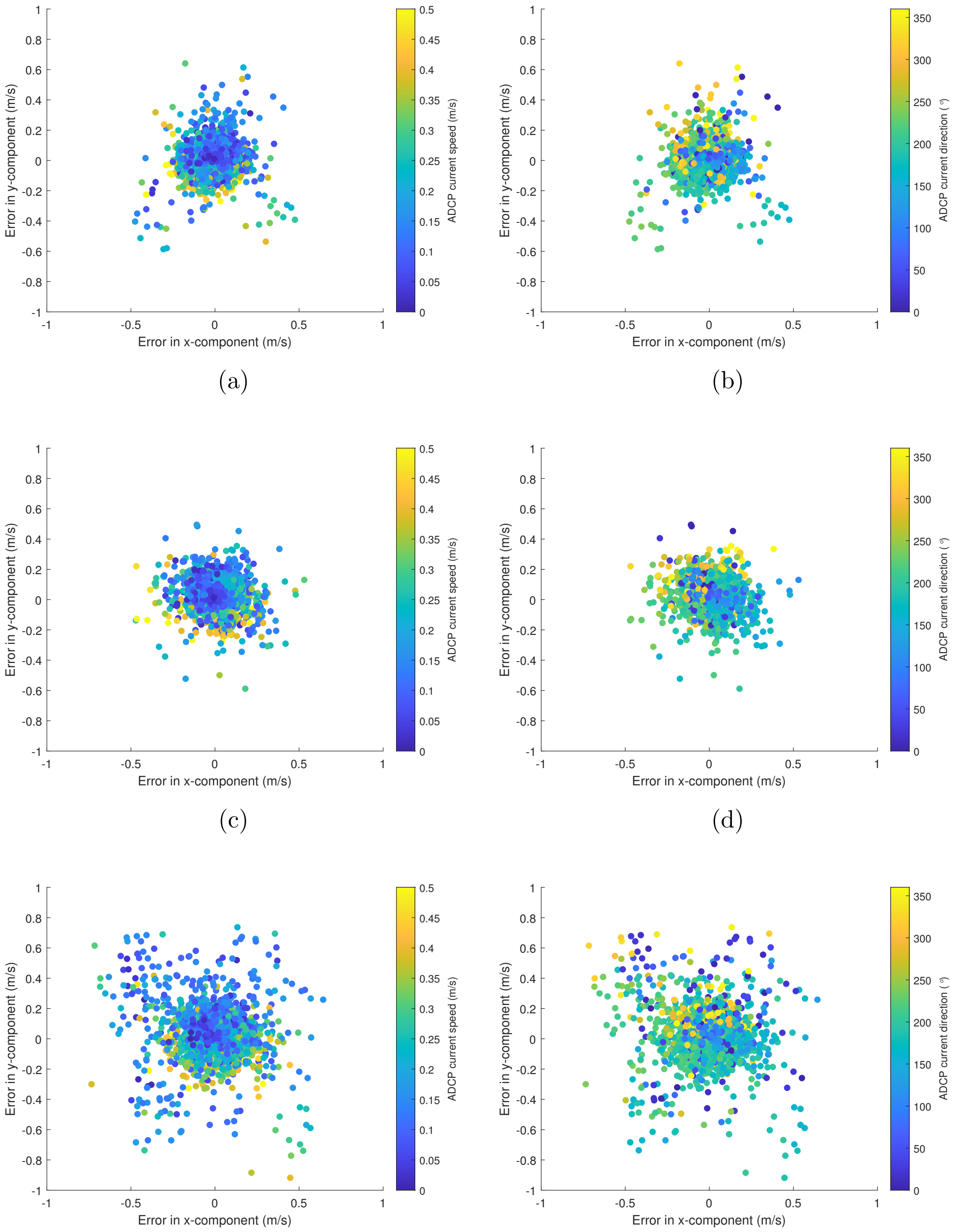

(a) (b)

(c) (d)

(e) (f)

Figure 3.12: Scatter plot of the difference in the east (x) and north (y) components of the current vector measured by ADCP and the radar along with the corresponding surface current speed using the (**a**) improved PCS, (**c**) PCS, and (**e**) NSP methods, as well as the corresponding surface current direction using the (**b**) improved PCS, (**d**) PCS, and (**f**) NSP methods.

3.6 Chapter Summary

In this chapter, an improved PCS algorithm [61] for retrieving surface currents from X-band marine radar images is presented. The improvements address several limitations of the original PCS method, particularly in the presence of noise, aliasing, and data outliers. By introducing filtering techniques and leveraging directional symmetry for noise reduction, the improved PCS method provides more accurate and reliable current estimates.

The analysis of the simulated data reveals that the improved PCS algorithm significantly enhances the accuracy of surface current retrieval, particularly at lower rotation speeds (RPM = 24). This improvement highlights the effectiveness of extracting reliable data points from the overall dataset, minimizing the influence of errors caused by curve fitting for individual wavenumber vectors. In real data applications, both the Decca radar data and the Koden radar data further validated the improved PCS algorithm. The comparison with ADCP reference data confirmed that the improved method achieved a higher CC and lower RMSD than the original method. Specifically, the improved PCS method has a speed CC of 0.85 and an RMSD of 0.08 m/s for the Decca data and a 15% reduction in the RMSD and a 12% improvement in the CC compared to the original PCS methods for the data collected by the Koden radar, which are better results than for the original PCS and NSP methods.

According to [10,62], wind-driven Ekman flows strongly influence currents within the top 10 m, and the current gradually changes direction and its speed decreases as depth increases. Thus, the ADCP current direction and speed depend on the depth of measurements. X-band radars provide an estimation of current close to the surface. Unfortunately, ADCP data for the top 10 m were unavailable. As a result, only the ADCP data at a depth of 11.2 m were utilized for comparison, despite ADCP measurements being available for depths ranging from 11.2 m to 150 m. This selection was because 11.2 m was the shallowest depth available in the dataset and measurements at greater depths tend to show larger differences from radar-derived currents due to the influence of subsurface dynamics that differ significantly from surface conditions. Among the available depths, the data at 11.2 m showed the closest alignment with the radar-derived results, further supporting its suitability for comparison in this study. The difference between the radar-derived current and ADCP sub-surface data can be partially attributed to the difference in the depths of their measurement.

While the difference between the improved and original PCS algorithms is less pronounced at higher rotation speeds (RPM = 48) in the simulated data, the Koden radar dataset (also RPM = 48) still shows slight improvements with the improved PCS method. The presence of noise and other real-world factors such as wave-current interactions, atmospheric conditions, and radar system imperfections in the Koden data allows the improved PCS algorithm to demonstrate the value of its individual steps, even in cases where the overall dataset quality is low. The ability of the improved PCS method to maintain accuracy in these conditions highlights its robustness against environmental noise and other data inconsistencies that affect current estimation.

In conclusion, the improved PCS method represents an advancement over traditional methods. It is more robust in real-world applications, where environmental noise and data anomalies are more common. This method may experience reduced effectiveness when the data quality is poor or when there is a lack of significantly concentrated wave energy. In such cases, the algorithm's ability to accurately retrieve ocean currents can be diminished, as it relies heavily on the presence of strong and coherent wave signatures to filter noise and perform accurate estimations. However, even under these conditions, its accuracy remains superior to other methods. Nevertheless, it is crucial to develop improved algorithms to better mitigate these limitations and further enhance performance in such challenging scenarios. Further improvements might focus on handling low-quality data and testing the robustness of the proposed method under varying sea states.

Chapter 4

Conclusion

4.1 Summary

This thesis focused on the development and enhancement of novel algorithms to improve the retrieval of ocean surface currents from X-band radar images. The motivation behind this research stemmed from the limitations of existing methods, particularly their sensitivity to noise and the decline in accuracy under certain challenging sea states. To address these issues, two new approaches were introduced and rigorously tested.

In Chapter 2, the first algorithm, known as the SDS Method, was presented. This method leverages the symmetrical properties of ocean waves, using the symmetry of Doppler shifts in the wavevector plane to estimate current velocities. By taking advantage of these symmetries, the SDS algorithm effectively reduces the influence of environmental noise, especially under low sea states, where traditional methods often experience difficulty.

The SDS algorithm was tested extensively using both simulated radar data and real-world datasets. In simulated environments, the method demonstrated strong performance, showing significant improvements in the accuracy of current speed and direction estimation compared to conventional techniques. The RMSD for current speed and direction were considerably lower, and the algorithm consistently performed better in environments with weaker wave activity. However, despite its robustness in simulations, the SDS method exhibited limitations when applied to real-world datasets. The irregularity of natural sea states, coupled with unpredictable noise sources, reduced the algorithm's effectiveness. In particular, under complex wave conditions and highly variable sea states, the symmetrical assumptions of the method did not hold as well, leading to reduced accuracy in current retrieval. Thus, the SDS algorithm was not directly applied to real-world datasets in Chapter 2 due to the significant noise and variability present in the raw data, which exceeded the assumptions and limitations of the method. It is difficult for the SDS method to achieve reliable results from the real radar data without additional preprocessing or filtering. In Chapter 3, a refined approach was introduced, where preprocessing techniques were applied to filter out noise and address the complexities of real-world conditions. This preprocessing enabled the SDS idea to be successfully incorporated to filter real-world data, demonstrating its potential for practical application under controlled conditions.

To overcome these limitations, Chapter 3 introduced a more advanced algorithm that integrates the symmetry-based method with an enhanced version of the PCS Method. This hybrid approach was designed to capitalize on the strengths of the SDS method while addressing its weaknesses, particularly in real-world conditions.

Key innovations in this combined approach include the incorporation of KDE for identifying high-density directions in the radar spectra, which helps to filter out noise and improve the accuracy of current estimations. Additionally, the use of IQR filtering allowed for more effective removal of outliers, ensuring that noisy data did not distort the final results. Finally, a unified curve-fitting process was introduced to standardize the estimation across all filtered data points, providing greater consistency and accuracy, especially when dealing with complex wave patterns.

The validation of this hybrid algorithm was carried out using both simulated and real-world radar datasets. In simulated tests, the hybrid method maintained the high accuracy observed in the SDS approach while improving upon the ability to handle noise and outliers.

In real-world datasets, the hybrid method demonstrated substantial improvements over both the standalone SDS and the original PCS methods. Notably, the hybrid approach showed a marked reduction in RMSD for current speed and direction estimates, and higher correlation coefficients, highlighting its effectiveness in more diverse and challenging conditions. Specifically, when tested on the 2008 Decca radar data and the 2017 Koden radar data, the hybrid method outperformed previous techniques, reducing speed estimation errors by 0.06 m/s and direction errors by 3.8° in the Decca dataset.

The results from the real-world tests demonstrated that the hybrid algorithm is not only capable of performing well in low-noise environments but also robust enough to handle the complexities of natural ocean conditions. This represents a significant improvement in the field of ocean surface current estimation, where accuracy is often compromised by environmental factors such as noise, wave irregularities, and challenging sea states.

In conclusion, the research presented in this thesis has contributed two important advancements in the field of radar-based surface current estimation. The Symmetry-Based Doppler Shift Method offers a novel way to reduce the influence of noise and enhance accuracy in controlled, simulated environments. However, its limitations in real-world conditions necessitated the development of the second, more robust algorithm. The Hybrid PCS-SDS Algorithm overcomes these challenges by combining advanced filtering techniques and a unified curve-fitting process, demonstrating superior performance across both simulated and real-world datasets.

4.2 Future Work

While this thesis has made some advancements in the accuracy and reliability of ocean surface current retrieval from X-band radar data, there are several promising directions for future research. Noise filtering techniques, though improved in this thesis with the use of KDE and symmetry-based filtering, can be further refined. For example, advanced machine learning algorithms such as convolutional neural networks (CNNs) could be employed to better identify and filter out noise patterns in radar images. Additionally, wavelet-based denoising methods could be explored to more effectively separate signal from noise across different frequency scales. The improved PCS method may experience reduced effectiveness when the data quality is poor or when there is a lack of significantly concentrated wave energy. In such cases, the algorithm's ability to accurately retrieve ocean currents can be diminished, as it relies heavily on the presence of strong and coherent wave signatures to filter noise and perform accurate estimations. However, even under these conditions, its accuracy remains superior to other methods. Nevertheless, it is crucial to develop improved algorithms to better mitigate these limitations and further enhance performance in such challenging scenarios. Further improvements might focus on handling low-quality data.

Another area worth exploring is the integration of the developed algorithms with other remote sensing technologies, such as HF radar, satellite altimetry, or SAR. Combining data from multiple sources could provide a more comprehensive and detailed view of ocean dynamics, improving both spatial and temporal coverage for current monitoring. Additionally, the optimization of these algorithms for real-time processing remains a challenge. Future work could focus on enhancing the computational efficiency of the methods, such as through parallelization, GPU acceleration, or cloud computing integration, allowing them to be deployed in operational systems for real-time marine and coastal monitoring. Another area worth exploring is the integration of the developed algorithms with other remote sensing technologies, such as HF radar, satellite altimetry, or SAR. Combining data from multiple sources could provide a more comprehensive and detailed view of ocean dynamics, improving both spatial and temporal coverage for current monitoring.

Bibliography

[1] N. Lucas, J. Simpson, T. Rippeth, and C. Old, “Measuring turbulent dissipation using a tethered ADCP,” *J. Atmos. Ocean. Technol.*, vol. 31, pp. 1826–1837, 2014.

[2] R. Bourgerie, T. Garner, and H. Shih, “Coastal current measurements using an ADCP in a streamlined sub-surface mooring buoy,” in *Proc. OCEANS ’02 MTS/IEEE*, vol. 2, Biloxi, MI, USA, 29-31 October 2002, pp. 736–741.

[3] R. A. Weller and R. E. Davis, “A vector measuring current meter,” *Deep-Sea Res. I: Oceanogr. Res. Pap.*, vol. 27, no. 7, pp. 565–581, 1980.

[4] E. W. Blockley, M. J. Martin, and P. Hyder, “Validation of foam near-surface ocean current forecasts using lagrangian drifting buoys,” *Ocean Sci.*, vol. 8, no. 4, pp. 551–565, 2012.

[5] W. Krauss, J. Dengg, and H. Hinrichsen, “The response of drifting buoys to currents and wind,” *J. Geophys. Res.*, vol. 94, pp. 3201–3210, 1989.

[6] H.-H. Essen, K.-W. Gurgel, and T. Schlick, “On the accuracy of current measurements by means of HF radar,” *IEEE J. Ocean. Eng.*, vol. 25, no. 4, pp. 472–480, 2000.

[7] K. Hickey, R. Khan, and J. Walsh, “Parametric estimation of ocean surface currents with HF radar,” *IEEE J. Ocean. Eng.*, vol. 20, no. 2, pp. 139–144, 1995.

[8] Y. Quilfen and B. Chapron, “Ocean surface wave-current signatures from satellite altimeter measurements,” *Geophys. Res. Lett.*, vol. 46, no. 1, pp. 253–261, 2019.

[9] L. Shemer, M. Marom, and D. Markman, “Estimates of currents in the nearshore ocean region using interferometric synthetic aperture radar,” *J. Geophys. Res. Oceans*, vol. 98, no. C4, pp. 7001–7010, 1993.

[10] B. Lund, H. C. Graber, H. Tamura, C. O. Collins III, and S. M. Varlamov, “A new technique for the retrieval of near-surface vertical current shear from marine X-band radar images,” *J. Geophys. Res. Oceans*, vol. 120, no. 12, pp. 8466–8486, 2015.

[11] W. Huang, X. Liu, and E. W. Gill, “Ocean wind and wave measurements using X-band marine radar: A comprehensive review,” *Remote Sens.*, vol. 9, no. 12, 2017, Art. no. 1261.

[12] X. Liu, W. Huang, and E. W. Gill, “Wind direction estimation from rain-contaminated marine radar data using the ensemble empirical mode decomposition method,” *IEEE Trans. Geosci. Remote Sens.*, vol. 55, no. 3, pp. 1833–1841, 2017.

[13] S. P. Neill and M. R. Hashemi, “In situ and remote methods for resource characterization,” in *Fundamentals of Ocean Renewable Energy.* New York, NY, USA: Academic Press, 2018, pp. 157–191.

[14] C. Shen, W. Huang, E. W. Gill, R. Carrasco, and J. Horstmann, “An algorithm for surface current retrieval from X-band marine radar images,” *Remote Sens.*, vol. 7, no. 6, pp. 7753–7767, 2015.

[15] F. Serafino, C. Lugni, and F. Soldovieri, “A novel strategy for the surface current determination from marine X-band radar data,” *IEEE Geosci. Remote. Sens. Lett.*, vol. 7, no. 2, pp. 231–235, 2010.

[16] Z. Yang, W. Huang, and X. Chen, “Evaluation and mitigation of rain effect on wave direction and period estimation from X-band marine radar images,” *IEEE J. Sel. Top. Appl. Earth Obs. Remote Sens.*, vol. 14, pp. 5207–5219, 2021.

[17] Z. Yang, W. Huang, and X. Chen, “Mitigation of rain effect on wave height measurement using X-band radar sensor,” *IEEE Sens. J.*, vol. 22, no. 6, pp. 5929–5938, 2022.

[18] L.-C. Wu, D.-J. Doong, and J.-W. Lai, “Sea surface current estimation from a semi-enclosed bay using coastal X-band radar images,” *IEEE Trans. Geosci. Remote Sens.*, vol. 62, 2024, Art. no. 4210511.

[19] I. R. Young, W. Rosenthal, and F. Ziemer, “A three-dimensional analysis of marine radar images for the determination of ocean wave directionality and surface currents,” *J. Geophys. Res.-Oceans*, vol. 90, no. C1, pp. 1049–1059, 1985.

[20] C. Senet, J. Seemann, and F. Ziemer, “The near-surface current velocity determined from image sequences of the sea surface,” *IEEE Trans. Geosci. Remote Sens.*, vol. 39, no. 3, pp. 492–505, 2001.

[21] R. Gangeskar, “Ocean current estimated from X-band radar sea surface images,” *IEEE Trans. Geosci. Remote Sens.*, vol. 40, no. 4, pp. 783–792, 2002.

[22] C. M. Senet, J. Seemann, S. Flampouris, and F. Ziemer, “Determination of bathymetric and current maps by the method disc based on the analysis of nautical X-band radar image sequences of the sea surface (november 2007),” *IEEE Trans. Geosci. Remote Sens.*, vol. 46, no. 8, pp. 2267–2279, 2008.

[23] Z. Chen, B. Zhang, V. Kudryavtsev, Y. He, and X. Chu, “Estimation of sea surface current from X-band marine radar images by cross-spectrum analysis,” *Remote Sens.*, vol. 11, no. 9, 2019, Art. no. 1031.

[24] B. Lund, C. Collins III, H. Graber, and E. Terrill, “On the imaging of surface gravity waves by marine radar: Implications for a moving platform,” in *Proc. 13th International Workshop on Wave Hindcasting and Forecasting and 4th Coastal Hazard Symposium*, Banff, AB, Canada, 27 October-1 November 2013.

[25] P. Bell and J. Osler, “Mapping bathymetry using X-band marine radar data recorded from a moving vessel,” *Ocean Dyn.*, vol. 61, pp. 2141–2156, 2011.

[26] B. Lund, H. C. Graber, K. Hessner, and N. J. Williams, “On shipboard marine X-band radar near-surface current 'calibration',” *J. Atmos. Ocean. Technol.*, vol. 32, no. 10, pp. 1928–1944, 2015.

[27] R. Gangeskar, “Verifying high-accuracy ocean surface current measurements by X-band radar for fixed and moving installations,” *IEEE Trans. Geosci. Remote Sens.*, vol. 56, no. 8, pp. 4845–4855, 2018.

[28] Y. Li and W. Huang, “Analyzing sources of inaccuracy in ocean surface current estimation from shipborne marine X-band radar data,” in *Proc. OCEANS 2024 MTS/IEEE - Halifax*, 2024, pp. 1–5.

[29] W. Huang, E. Gill, and J. An, “Iterative least-squares-based wave measurement using X-band nautical radar,” *IET Radar, Sonar Navig.*, vol. 8, no. 8, pp. 853–863, 2014.

[30] J. C. Nieto-Borge, K. Hessner, and P. Jarabo-Amores, “Signal-to-noise ratio analysis to estimate ocean wave heights from X-band marine radar image time series,” *IET Radar Sonar Navig.*, vol. 2, no. 1, pp. 35–41, 2008.

[31] Z. Yang and W. Huang, “Wave height estimation from X-band radar data using variational mode decomposition,” *IEEE Geosci. Remote. Sens. Lett.*, vol. 19, 2022, Art. no. 1505405.

[32] Z. Yang and W. Huang, “SWHFormer: A vision transformer for significant wave height estimation from nautical radar images,” *IEEE Trans. Geosci. Remote Sens.*, vol. 62, 2024, Art. no. 5104213.

[33] P. H. Y. Lee, J. D. Barter, K. L. Beach, C. L. Hindman, B. M. Lake, H. Rungaldier, J. C. Shelton, A. B. Williams, R. Yee, and H. C. Yuen, “X band microwave backscattering from ocean waves,” *J. Geophys. Res.*, vol. 100, no. C2, pp. 2591–2611, 1995.

[34] W. Plant and W. Keller, “Evidence of Bragg scattering in microwave doppler spectra of sea return,” *J. Geophys. Res.*, vol. 95, no. C9, pp. 16 299–16 310, 1990.

[35] J. Borge and C. Soares, "Analysis of directional wave fields using X-band navigation radar," *Coast. Eng.*, vol. 40, no. 4, pp. 375–391, 2000.

[36] J. MacQueen, "Some methods for classification and analysis of multivariate observations," in *Proc. 5th Berkeley Symp. Math. Statist. Probab.*, vol. 1, 1967, pp. 281–297.

[37] W. J. Pierson and L. Moskowitz, "A proposed spectral form for fully developed wind seas based on the similarity theory of A. A. Kitaigorodskii." *J. Geophys. Res.*, vol. 69, pp. 5181–5190, 1964.

[38] D. H. Nomiyama and T. Hirayama, "Evaluation of marine radar as an ocean-wave-field detector through full numerical simulation," *J. Mar. Sci. Technol.*, vol. 8, no. 2, pp. 88–98, Oct. 2003.

[39] W. Huang and E. Gill, "Simulation analysis of sea surface current extraction from microwave nautical radar images," in *Proc. IEEE ICIP*, Orlando, FL, USA, 30 September–3 October 2012, pp. 2673–2676.

[40] J. C. Nieto-Borge, G. R. RodrÍguez, K. Hessner, and P. I. González, "Inversion of marine radar images for surface wave analysis," *J. Atmos. Ocean. Technol.*, vol. 21, no. 8, pp. 1291–1300, 2004.

[41] J. Röhrs, G. Sutherland, G. Jeans, M. Bedington, A. K. Sperrevik, K.-F. Dagestad, Y. Gusdal, C. Mauritzen, A. Dale, and J. H. LaCasce, "Surface currents in operational oceanography: Key applications, mechanisms, and methods," *J. Oper. Oceanogr.*, vol. 16, no. 1, pp. 60–88, 2023.

[42] A. Lane, P. Knight, and R. Player, "Current measurement technology for near-shore waters," *Coastal Eng.*, vol. 37, no. 3, pp. 343–368, 1999.

[43] D. E. Barrick, M. W. Evans, and B. L. Weber, "Ocean surface currents mapped by radar," *Science*, vol. 198, no. 4313, pp. 138–144, 1977.

[44] W. Wang, E. W. Gill, and W. Huang, "Comparison of spectral estimation methods for rapidly varying currents obtained by high-frequency radar," *IEEE J. Ocean. Eng.*, vol. 42, no. 3, pp. 556–565, 2017.

[45] L. Novi, F. Raffa, and F. Serafino, "Comparison of measured surface currents from high frequency (HF) and X-band radar in a marine protected coastal area of the ligurian sea: Toward an integrated monitoring system," *Remote Sens.*, vol. 12, no. 18, 2020, Art. no. 3074.

[46] P. Izquierdo and C. Guedes Soares, "Analysis of sea waves and wind from X-band radar," *Ocean Eng.*, vol. 32, no. 11, pp. 1404–1419, 2005.

[47] X. Chen and W. Huang, "Spatial-temporal convolutional gated recurrent unit network for significant wave height estimation from shipborne marine radar data," *IEEE Trans. Geosci. Remote Sens.*, vol. 60, 2022, Art. no. 4201711.

[48] W. Huang and E. Gill, "Surface current measurement under low sea state using dual polarized X-band nautical radar," *IEEE J. Sel. Top. Appl. Earth Obs. Remote Sens.*, vol. 5, no. 6, pp. 1868–1873, 2012.

[49] S. Wang and C.-K. Rheem, "Research on optimal machine learning algorithm for sea surface observation using X-band doppler radar," in *Proc. OCEANS 2023 MTS/IEEE*, Limerick, Ireland, 5–8 June 2023, pp. 1–6.

[50] K. G. Hessner, S. El Naggar, W.-J. von Appen, and V. H. Strass, "On the reliability of surface current measurements by X-band marine radar," *Remote Sens.*, vol. 11, no. 9, 2019, Art. no. 1030.

[51] M. H. Derkani, A. Alberello, F. Nelli, L. G. Bennetts, K. G. Hessner, K. MacHutchon, K. Reichert, L. Aouf, S. Khan, and A. Toffoli, "Wind, waves, and surface currents in the southern ocean: observations from the antarctic circumnavigation expedition," *Earth Syst. Sci. Data.*, vol. 13, no. 3, pp. 1189–1209, 2021.

[52] W. Huang, R. Carrasco, C. Shen, E. W. Gill, and J. Horstmann, “Surface current measurements using X-band marine radar with vertical polarization,” *IEEE Trans. Geosci. Remote Sens.*, vol. 54, no. 5, pp. 2988–2997, 2016.

[53] F. E. Grubbs, “Procedures for detecting outlying observations in samples,” *Technometrics*, vol. 11, no. 1, pp. 1–21, 1969.

[54] S. R. Sain, “Multivariate locally adaptive density estimation,” *Comput. Stat. Data Anal.*, vol. 39, no. 2, pp. 165–186, 2002.

[55] B. W. Silverman, *Density estimation for statistics and data estimation.* London: Chapman and Hall, 1986.

[56] X. Wan, W. Wang, J. Liu, and T. Tong, “Estimating the sample mean and standard deviation from the sample size, median, range and/or interquartile range,” *BMC Med. Res. Methodol.*, vol. 14, no. 135, 2014.

[57] Y. Li and W. Huang, “An algorithm for ocean current inversion from X-band marine radar images,” in *Proc. 2024 IEEE Intl. Geosci. Remote Sens. Symp. (IGARSS)*, Athens, Greece, 7-12 July 2024, pp. 5956–5960.

[58] J. N. Borge, G. R. RodrÍguez, K. Hessner, and P. I. González, “Inversion of marine radar images for surface wave analysis,” *Journal of Atmospheric and Oceanic Technology*, vol. 21, no. 8, pp. 1291 – 1300, 2004.

[59] M. C. Haller, D. A. Honegger, R. Pittman, A. O’Dea, and A. Simpson, “Real-time marine radar observations of nearshore waves and flow structures from shore-based towers,” in *Proc. 2019 IEEE/OES Twelfth Current, Waves and Turbulence Measurement (CWTM)*, San Diego, CA, USA, 10–13 March 2019, pp. 1–7.

[60] J. A. Lerczak, J. A. Barth, J. Calantoni, J. A. Colosi, J. A. MacKinnon, J. N. Moum, A. F. Waterhouse, J. Thomson, J. M. McSweeney, J. Becherer, S. D. Pierce, C. Swann, R. S. Mieras, A. Palóczy, G. Voet, P. Chua, M. Stone, and P. Jessen, “Offshore moorings: moorings deployed in 10 m - 150 m water depth on the inner- to mid-shelf. in

observations and model simulations from the Inner-Shelf dynamics experiment (ISDE)," UC San Diego Library Digital Collections: La Jolla, CA, USA, 2022.

[61] Y. Li, Z. Yang, and W. Huang, "Improved polar current shell algorithm for ocean current retrieval from X-band radar data," *Remote Sens.*, vol. 16, no. 22, 2024, Art. no. 4140.

[62] V. W. Ekman, "On the influence of the earth's rotation on ocean currents," *Ark. Mat. Astron. Fys.*, vol. 2, pp. 1–53, 1905.